WAVELET APPROXIMATION AND IMAGE RESTORATION

LI JIA

(B.Sc., SYSU, China)

A THESIS SUBMITTED
FOR THE DEGREE OF DOCTOR OF PHILOSOPHY
DEPARTMENT OF MATHEMATICS
NATIONAL UNIVERSITY OF SINGAPORE
2013

DECLARATION

I hereby declare that the thesis is my original work and it has been written by me in its entirety.

I have duly acknowledged all the sources of information which have been used in the thesis.

This thesis has also not been submitted for any degree in any university previously.

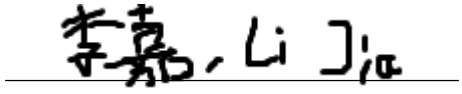

Li Jia
August 2013

Acknowledgements

At the very beginning, I would like to give my sincerest thanks to my advisor, Professor Shen Zuowei who has taught me not only the knowledge of wavelet tight frame but also the way of deep thinking and connective thinking. His theories of wavelet tight frames bring out a good structure to represent the piece-wise smooth images in our real life, which is very helpful for my research on various applications on image restorations and CT image reconstructions. Moreover, he illuminated me to find the relationship between the wavelet frame coefficients and the derivatives of smooth functions through the approximation theory, which lead me to develop the approximation theory in this thesis. Without his patient and systematical instruction and suggestion, I can hardly obtain my research results shown in this thesis.

Furthermore, his attitude of research and thinking problems has influenced me a lot and will be one of my totem in my future study and life. When I was just became his student three years ago, I was anxious for quick results and seldom curious with the deep reason of the results. I treated some of the complicated program code packages as a "black box" and only knew how to use them. Professor Shen rectified me and told me that one cannot go beyond his current level if he never deeply think about the reasons and the principles of everything he reads or observes. In my later theoretical research, Professor Shen also emphasized the importance of searching in broader range and linking different mathematics theories together. With several years' study and exercise, I have already possessed the habit of connective thinking although I still cannot link different theories very well.

I also need to thank all of my collaborators and friends, especially Professor

Wang Ge, Professor Ji Hui, Professor Yu Hengyong, Dr. Dong Bin, Dr. Xu Yuhong, Mr. Miao Chuang and Mr. Wang Kang, they helped me overcome all the difficulties in my research as a graduate student. In particular, Professor Ji Hui helped me to adjust the program style of MATLAB and gave me many helpful suggestions to clearly and powerfully express the key results. Additionally, I want to thank Ms. Carol Lam for her great contribution in modifying and polishing the language of this thesis.

At last, I would never forget to thank all my family members including my parents and my wife. Without everybody's love and good-to-excellent care, there would not be what I am today.

Contents

Summary

The image inpainting problem is to recover degraded images with partial image pixels being missing during transmission or damaged by impulsive noise. Most of the existing inpainting techniques require knowing beforehand where the damaged pixels are, either given as a priori or detected by some pre-processing. However, such information neither is available nor can be reliably pre-detected in some applications. As a result, by applying the wavelet regularization scheme, this thesis introduces two wavelet frame based blind inpainting models to simultaneously identify and recover the damaged pixels in the given corrupted images. Numerical experiments on various image restoration tasks: recovering images that are blurry and damaged by scratches, image denoising for noise mixed by both Gaussian and random-valued impulse noise, show that our method is compared favorably against the two-stage methods with pre-detecting of the damaged pixels.

As X-ray computed tomography (CT) is widely used in diagnosis of cancer and radiotherapy, it is important to reduce the radiation dose as low as reasonably achievable. For the CT image reconstruction problem, besides some popular un-regularized methods, such as filtered back projection (FBP) method and the simultaneous algebraic reconstruction technique (ART), total variation (TV) and wavelet tight frame regularization have been proposed to reconstruct high quality images from lower projection dose. This thesis proposed two types of isotropic wavelet frame based CT image reconstruction methods to reconstruct the object images with most features and least errors caused by noise and artifacts. Radon domain inpainting mechanism and three-system structure were introduced to the proposed methods to improve the robustness to the extremely insufficient measurement and the inaccurate projection

matrix P. Numerical simulations show that the proposed method can outperform the FBP method, TV based methods and an existing anisotropic wavelet frame based method in terms of visibility, relative error and mean structural similarity. The present study is able to preserve the quality of reconstructed images with less projection dose. Therefore, it is possible to reduce the X-ray exposure to the patients in clinical applications without decreasing the accuracy of diagnosis.

The wavelet frame regularization scheme performs well in both image inpainting and CT image reconstruction because of not only the representation of the singularities by wavelet coefficients but also the approximation of smooth image pieces by low frequency coefficients. In approximation theory, the quasi-projection operator has been a canonical and effective tool for almost forty years. It has been proved that given an appropriate set of functions, the quasi-projection operators can approximate smooth functions with high approximation order. In particular, quasi-projection operators based on B-spline refinable functions can approximate any smooth function with approximation order up to 2. This thesis has proved that the approximation to the derivatives of smooth functions can be realized by B-spline wavelets with arbitrarily high approximation order. The proof was deduced generally by constructing functions $\phi_{m,l,n}$ with which the integrated B-spline wavelets $\varphi_{m,l}$ can formulate a quasi-projector which can exactly reproduce higher order polynomials. The result of the proof show that the wavelet frame decomposition can approximate the function through different order of differential operators. Moreover, the improved approximation order in the proof can expand the application of B-spline wavelets to the approximation of complicated functions.

List of Tables

List of Figures

Chapter 1

Introduction

Nowadays, image restoration becomes more and more popular in signal transmission, scientific experiments and medical applications, etc. Usually, besides guaranteeing the fidelity, high quality restored images should preserve sharp edges, smooth pieces and textures while suppressing the additive noises. The wavelet tight frame decomposition (see [32, 68, 37]) can provide sparse representation of piece-wise smooth images. Moreover, the coefficients of wavelet decomposition can provide good approximation to underlying solutions and their derivatives in smooth pieces partitioned by sharp edges. Therefore, the regularization in wavelet transform domain is effective to obtain sparse solutions and clear images.

In this thesis, the wavelet tight frame will be introduced to two types of image restoration problems: image inpainting and computed tomography (CT) image reconstruction. Based on the split Bregman algorithm [50], the proposed wavelet frame based methods can be fast solved by PC in less than 5 minutes. The numerical results verified the superiority of wavelet frame based image restoration methods compared to other methods including the total variation (TV) based methods [69].

Additionally, this thesis also provided a proof showing that the coefficients of wavelet decomposition can form quasi-projection operators to approximate the smooth functions and their derivatives with arbitrarily high approximation order, which demonstrates the preservation of smooth pieces during the execution of frame regularized image restoration methods.

1.1 Background

This section is mainly devoted to the introduction of wavelet tight frames and their applications to image restorations and approximation theories. A countable set $X \subset L_2(\mathbb{R})$ is called a tight frame of $L_2(\mathbb{R})$ if

$$f = \sum_{h \in X} \langle f, h \rangle h \quad \forall f \in L_2(\mathbb{R}),$$

where $\langle \cdot, \cdot \rangle$ is the inner product of $L_2(\mathbb{R})$. Given a finite collection of functions $\Psi = \{\psi_1, \psi_2, ..., \psi_m\}$, define $X = \{\psi_{n,k,i} = 2^{n/2}\psi_i(2^n \cdot -k), 1 \leq i \leq m\, n, k \in \mathbb{Z}\}$. If X satisfies the condition of tight frame, then X can be called a wavelet tight frame and Ψ is called the wavelet. The multi-resolution analysis (MRA) based wavelet can be generated by the unitary extension principle (UEP) [68]. Given a 1-dimensional framelet system for $L_2(\mathbb{R})$, the s-dimensional tight wavelet frame system for $L_2(\mathbb{R}^s)$ can be similarly generated by using tensor products of 1-dimensional framelets (see e.g. [32, 37]).

In discrete sense, a discrete image u with totally s pixels is an s-dimensional array. In this thesis, W denotes the fast tensor product framelet decomposition and $W^\top$ denotes the fast reconstruction. Then by the unitary extension principle [68], we have $W^\top W = I$, i.e. $u = W^\top W u$ for any image u. We will further denote an L-level framelet decomposition of u as

$$Wu = \{W_{l,i,j}u : 1 \leq l \leq L, (i,j) \in I_0\},$$

where I_0 is the index set of all framelet bands and only $(i,j) = (0,0)$ represents the low-pass channel. In image processing models and algorithms, the singularities such as the sharp edges and noises, can be reflected by wavelet coefficients or high frequency coefficients. For most existed images in practice, the features such as sharp edges correspond to large wavelet coefficients while the locally smooth parts correspond to the wavelet coefficients equal or closed to zero. Therefore, for most image restoration problems, besides the given fidelity conditions, it is reasonable to approach a solution with sparse representation in the high-pass part of the wavelet transformed domain. In fact, all the proposed wavelet frame based image restoration models in Chapter 2 and 3 should include a regularization term $\|Wu\|_{1,p}$ for $p = 1, 2$ to approach sparse solutions. Numerically, the regularization term $\|Wu\|_{1,p}$ for

$p = 1, 2$ is realized through the soft thresholding operator defined by (2.10) which can preserve the large wavelet coefficients while removing the small ones. It should be remarked that such thresholding operation is a non-linear approximation since the κ-sparse vector subspace with $\kappa > 0$ is a non-linear space.

On the other hand, the sharp edges automatically make a partition of the image to several smooth pieces. For each smooth piece, the approximation of wavelet system guarantees that the low frequency coefficients $W_{l,0,0}$ provide a good approximation of the underlying function. Therefore, the information in each smooth piece of image can be preserved since the low frequency coefficients are not directly changed during the execution of frame based image restoration algorithms. Interested readers can refer to [76, 37] for more details about the wavelet tight frame and its applications.

In the following part of this section, the background of image inpainting problem and CT image reconstruction problem will be provided. Some basic concepts and definitions of wavelet approximation will be also given in the last part of this section.

1.1.1 Image Inpainting

The word "inpainting" was proposed by museum restoration artists and such word has been initially applied to digital image inpainting by [6]. In practice, there are many images degraded from missing or damaged pixels, e.g., the ancient drawings with missing portions by aging, the frame of old film which is damaged by scratching, or the images corrupted by impulse noise due to noisy sensors or channel transmission error. Thus, image inpainting methods are designed to estimate and recover the missing information within the missing/damaged regions from incomplete observation of the images which may even be in presence of Gaussian noise or other mixed noise. Regarding to the image inpainting problem, an ideal recovery of an image in the corrupted regions should possess the smooth regions, sharp edges, and periodical textures as these features observed. Moreover, it is necessary to suppress the noise and artifacts as much as possible in the inpainting result images. In recent years, the model and algorithm for image inpainting has been remarkably developed and improved. Interested readers can refer to [5, 6, 7, 26, 27, 24] for more details about the development and application for image inpainting problem. In particular, the wavelet frame regularization has also been successfully applied to the image inpainting problem as in [22, 10, 11, 12, 76, 37, 25].

Let an image be represented as a column vector in $\mathcal{R}^n$, where n is the total number of pixels. Then the image inpainting problem can be formulated as follows:

$$f(i) = \begin{cases} (Hu)(i) + \epsilon(i), & i \in \Lambda \\ v(i), & i \in \Lambda^c, \end{cases} \tag{1.1}$$

where f is the observed image with missing/damaged pixels, u is the true image for image inpainting problem, ϵ represents the additive noise which is most frequently chosen as the regular Gaussian noise with zero mean, H is some degradation matrix (identity operator for pure image inpainting and convolution operator for image blurring), and Λ is the index set of the correct pixels of the image. The random-valued vector v represents the intensity values of the missing/damaged pixels. The vector v defined on the index set of missing/damaged pixels Λ^c can represent the impulse noise (e.g. salt-and-pepper noise and random-valued impulse noise) or random scratches with unknown intensities. The goal of the image inpainting is then to estimate the original image u from the observation f.

The index set $\Lambda^c = \text{supp}(v)$ is referred to as the inpainting domain or the position/region/domain of the missing/damaged pixels. In practice, the index set Λ^c is usually given as prior knowledge or estimated beforehand using some numerical detectors. With the true value or well estimated value of Λ^c, it is not a difficult problem to reconstruct the true image u from f with high peak signal-to noise (PSNR) value even if the proportion of Λ^c is over 20%.

In some applications, however, the inpainting domain may not be readily available, or the detection of the Λ^c may have huge error by some separate process, *e.g.* when the vector v in (1.1) is formed from random-valued impulse noise or scratch with unknown intensities. As a result, the image inpainting problem without knowing of Λ^c is called the *blind inpainting* problem. Compared with the regular or *non-blind inpainting* problems in which the index set Λ is generally known, it is necessary to estimate both the index set Λ and the true image u in blind inpainting problem from merely the observation f, which formulate a highly ill-posed inverse problem.

1.1.2 Computed Tomography Image Reconstructions

In two dimensional case, the most common CT system is the fan-beam CT system whose X-ray source is assumed as a point. This thesis will always focus on

the fan-beam scanning geometry with the source and detector revolving around the object in a fixed radius by 360 degrees. For a given angle θ and beamlet r, the X-ray projection operator $P^{\theta,r}$ is defined as follows:

$$P^{\theta,r}[u] = \int_0^{L(r)} u(\mathbf{x}_\theta + \mathbf{n}l)dl,$$

where u is the unknown two dimensional true image (X-ray attenuation coefficients), $\mathbf{x}_\theta = (x_\theta, y_\theta)$ represents the cartesian coordinate of the X-ray source for each projection angle θ, $\mathbf{n} = (n_x, n_y)$ is the direction vector of beamlet r, and $L(r)$ is the length of the X-ray beamlet from the source to the corresponding intersection on the imager. If $P^{\theta,r}[u]$ is sampled with respect to different beamlet r for each angle θ, the resulting data projection can essentially be written as a vector f_θ. By collecting f_θ together for all different angles θ, we obtain an image denoted as f whose columns are formed by f_θ. An example of simulated NCAT phantom is shown in Figure 1.1.

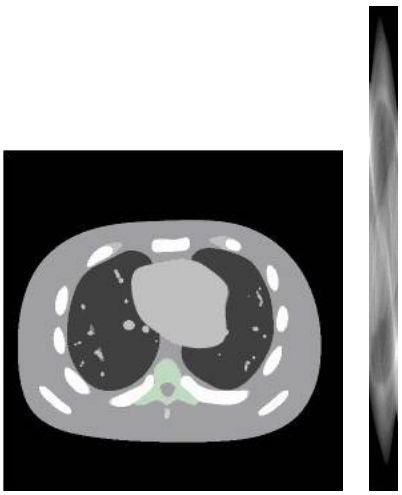

Figure 1.1: The NCAT phantom and its corresponding measurement image f with 30 different projection angles.

With appropriate discretization of the the true image u, we can reinterpret the CT image reconstruction problem as a linear inverse problem

$$Pu = f,$$

where P is a matrix represents the collection of discrete line integrations $P^{\theta,r}$ with different θ and r. In other words, the CT image reconstruction problem is essentially to recover image u from its partial Radon transform f (see [67] for the details of

Radon transform). Since the matrix P only depends on the location and direction of each beamlet and is irrelevant to u, we can construct the huge sparse matrix P beforehand. In this thesis, the matrix P is generated by Siddon's algorithm [78] which calculates the length of beamlet in each discrete image pixel.

In the CT reconstruction from real projection data, however, due to the error caused by the imaging equipment itself, the actual measurement f does not equal to Pu. In fact, the reconstruction problem can be redefined as:

$$(P + P_\delta)u = f + \epsilon, \tag{1.2}$$

where P_δ represents the error of the projection matrix P caused by the error of beamlet location and direction, and ϵ is the additive noise. Besides these instrument error, insufficient projections or detector cells will cause the matrix P highly undetermined, i.e. the matrix has much smaller number of rows comparing to the number of columns. Therefore, it is difficult to identify the most appropriate u from infinitely many solutions of the problem (1.2).

The current CT reconstruction methods can be categorized as un-regularized methods or regularized methods. In the following part of this subsection, I will briefly introduce two popular un-regularized methods and a regularized method named total variation (TV) regularized method. In some sense, these methods lead to the motivation of designing our models and algorithms.

The most classical and most commercially used CT reconstruction method is the filtered back projection (FBP) method [44, 35, 64, 60] which is an un-regularized method and first proposed in 1980s. Independently, the algebraic reconstruction technique (ART) [51], another un-regularized method, is the earliest method based on solving the linear system $Pu = f$ by some simple methods such as the least square method. Both the above methods use linear transform to the initial measurement and the true image can be reconstructed by these methods with sufficient measurement. However, these methods are zero robust to the instrument error and the additive noise which can apparently reduce the quality of the reconstructed images. What is worse, these methods usually suffer from different shapes of artifacts especially when the amount of measurement is insufficient.

To suppress noise and artifacts while preserving the features of the reconstructed images, various differential operator based regularized methods have been proposed,

among which the total variation (TV) regularized method is one of the most well-known models and is proven to be effective both in theories and experiments. The TV regularized model (known as the ROF model) was historically proposed by [69] in the context of image denoising. Illuminated by the theoretical proof and experiment results in [69], TV regularized method has been extended and applied to other image processing and analysis tasks such as in [62, 70, 65, 19, 25]. In particular, the TV regularized method has been initially applied to 3D X-ray cone beam CT reconstruction in [80, 79] and later applied to 2D CT reconstruction in [59]. The canonical form of TV-based CT reconstruction model is defined as follow:

$$\min_u \quad \frac{1}{2}\|Pu - f\|_2^2 + \lambda\|\nabla u\|_1. \tag{1.3}$$

where the operator ∇ is the discretization of 2D gradient operator. The first term $\frac{1}{2}\|Pu - f\|_2^2$ is called the fidelity term since it guarantees that $Pu \approx f$. The second term $\lambda\|\nabla u\|_1$ is the regularization term which lead the solution u to be piecewise constant. The parameter λ is determined by the noise level of the measurements and the smoothness of the estimated object images.

Compared with the un-regularized methods, TV regularized method tends to reconstruct piecewise constant images while most medical true images are piecewise smooth, which is close to piecewise constant. Therefore, TV can roughly estimate the true image with insufficient measurement in the presence of additive noise. However, due to the simple regularization structure and lower approximation order, the TV regularized method is likely to oversmooth the result images. As a result, some important features which cannot be distinguished from noise and artifacts might also be removed during the process of CT reconstruction, which is generally unacceptable in clinical applications. Therefore, better regularization scheme is necessary for pursuing higher quality result images for CT reconstruction problem as well as other image restoration problems.

Fortunately, the generation of wavelet tight frames [32, 68, 33] and its related framelets is a historical progress for better structure of regularization scheme. Similar to the TV regularized model (1.3), the wavelet frame based approaches can be applied to CT image reconstruction problem. Moreover, it has been shown in [13] that one of the wavelet frame based approaches, named analysis based approach, can be regarded as a finite difference approximation of a certain type of general variational model, and such approximation will be exact when the image resolution

goes to infinity. On the contrary, owing to the multi-resolution structure and redundancy of wavelet frames, wavelet frame based models can adaptively choose a proper differential operators in different regions for a given image according to the order of the singularity of the underlying solutions. As a result, the discretizations provided by wavelet frames were always shown to be superior than the standard discretizations for the TV-based model (1.3) in [58, 36] for CT reconstruction problem and in [20, 22, 13, 37] for other general image restoration problems.

Note that wavelet based image restorations include three different kinds of approaches, namely the synthesis based, analysis based and balanced approaches [20, 21]. The balanced approach is the one that balances the synthesis based and analysis based approaches. In [36], it has been shown that the analysis based approach outperforms other wavelet based approaches in terms of relative error and correlations. The analysis based approach regularization can be defined as in (1.4):

$$\min_u \quad \frac{1}{2}\|Pu - f\|_2^2 + \lambda\|Wu\|_{1,p}, \tag{1.4}$$

where the norm $\|\cdot\|_{1,p}$ is defined as

$$\|Wu\|_{1,p} = \left\| \sum_{l=1}^{L} \Big(\sum_{(i,j)\neq(0,0)} |W_{l,i,j}u|^p \Big)^{\frac{1}{p}} \right\|_1, \quad p = 1, 2.$$

When $p = 1$, the norm $\|\cdot\|_{1,1}$ is referred to as the *anisotropic* ℓ_1-norm which is the standard ℓ_1-norm used for frame based image restoration problems. When $p = 2$, the norm $\|\cdot\|_{1,2}$ is referred to as the *isotropic* ℓ_1-norm of the frame coefficients. In [36] it has been shown that the isotropic ℓ_1-norm regularization performs better in CT reconstruction problems, which coincides with the theoretical analysis in [13].

1.1.3 Approximation

The quasi-projection (or quasi-interpolatory) operator of ϕ can be defined as:

$$P_j f = 2^j \sum_{\alpha\in\mathbb{Z}} \langle f, \phi(2^j \cdot -\alpha)\rangle \phi(2^j \cdot -\alpha) \qquad f \in L_2(\mathcal{R}),$$

where $\phi(2^j \cdot -\alpha)$ represent the function ϕ with integer shift α and dilation 2^j. Then the quasi-projection operator P_j provides approximation order n if

$$\|f - P_j f\|_2 = O(2^{-nj}), \tag{1.5}$$

where the function f may be restricted in some smooth spaces such as the Sobolev spaces $W_p^s(\mathcal{R})$ with differential order $s \geq n$.

The construction of various wavelet tight frames through the unitary extension principle (UEP) was first provided in [68], in which the B-spline wavelet tight frame can provide an approximation order never larger than 2 because the condition $1 - |\hat{\phi}|^2 = O(|\cdot|)^n, n > 2$ is not hold if ϕ is merely the B-spline refinable functions. In order to construct wavelet tight frames with satisfactory approximation order of truncated frame series, the wavelet tight frames based on pseudo-splines were generated in [33, 74]. The pseudo-splines, defined as a linear combination of finite shifted B-spline functions, can bring out better quasi-projection operator P_r with arbitrarily high approximation order for smooth functions [33]. The progress is made by approaching the Strang-Fix condition and the approximation condition $1 - |\hat{\phi}|^2 = O(|\cdot|)^n$ with higher n. The detail of deduction from such two conditions to (1.5) has been provided in [56, 37]. It should be remarked here that all the above wavelet tight frames are all based on multi-resolution analysis (MRA) generated by a refinable function $\phi \in L_2(\mathcal{R})$.

1.2 The Goal and Contribution of the Thesis

Based on the existing application of wavelet tight frame to image restorations, this thesis proposed some new wavelet frame based methods to solve the image inpainting problems and CT image reconstruction problems. In the proposed methods, the multi-system method, which is based on different image parts having sparse representation in different domains, is applied to separate the image into the cartoon part, texture part, artifacts part and additive noise part. In particular, the cartoon part and texture part should be contained in the restored image and the remaining part should be discarded. Moreover, the isotropic wavelet frame regularization [13], which treats the singularities in different directions equally, is also applied in the proposed CT reconstruction methods. Moreover, the Radon domain

inpainting mechanism is introduced for CT image reconstruction from highly insufficient measurement. By using split Bregman algorithm, the proposed analysis based approach method can be solved fast. The numerical simulations show that the proposed method outperforms the existing wavelet frame based methods and other image restoration methods.

Regarding to the approximation of wavelet tight frame system, besides the revision of quasi-projection operators and the approximation of smooth functions by low frequency coefficients, this thesis provided a proof to show that the wavelet coefficients, or the high frequency coefficients, can approximate the derivatives of underlying functions. Moreover, with the appropriate designation of dual functions, the approximation order of smooth functions and their derivatives can be arbitrarily high. The result of the proof will demonstrate that in smooth pieces of images, the thresholding operation of high frequency coefficients which occurs in majority of wavelet frame based image restoration methods, can preserve most of the intensity information in the restored images.

1.2.1 Blind Image Inpainting

One goal of the thesis is to develop some novel computational models and corresponding efficient algorithms for solving the blind image inpainting problem without priori knowledge of the index set Λ of the missing/damaged pixels. A Lagrangian regularization approach will be used for the designation of the proposed blind inpainting methods. In order to overcome the ill-posedness of the problem, i.e, lacking the information of Λ, appropriate regularization terms on both the original image u and the inpainting region Λ^c are necessary in the minimization problem. The basic idea of our method is to utilize the sparsity priors of images and random-valued vector v in different domains. Due to the success of applying sparsity prior of images under tight wavelet frames in many image restoration tasks ([30, 17, 16, 28, 34, 41, 43, 18, 11, 76, 37]), our approach set the ℓ_1 norm of wavelet tight frame coefficients of images is used as the regularization term. On the other hand, since the inpainting domain Λ^c is nothing but the support of v, the regularization on Λ^c can be done by regularizing the supp(v). Therefore, with the assumption that v is sparse in spatial domain, we include the ℓ_1 norm of v in spatial domain as the regularization term in our optimization model. Moreover, similar as the CT reconstruction problem, the proposed minimization problem can be efficiently solved

via the split Bregman algorithm. The split Bregman algorithm first proposed in [50] has already been proved to be successful in various image processing applications such as [50, 49, 15]. The detailed form of the proposed models and the corresponding algorithms can be seen in Section 2.1.

1.2.2 CT Image Reconstructions from Lower X-Ray Dose

Despite the progress made by isotropic wavelet frame regularization, it is still impossible to reconstruct high quality images from very small number of projection angles by the model (1.4), let alone the un-regularized methods and TV regularized methods. In order to preserve the CT reconstruction quality with even smaller number of projection angles, this thesis will introduce a Radon domain inpainting mechanism which inpaints with respect to projection angles. For example, Figure 1.2 shows that the Radon domain inpainting mechanism can approximate the measurement f with 20 projection angles (as the number of columns in Figure 1.2) from the actual measurement f_0 which only include 10 projections (as the even columns of f). Although the 10 additional projections are merely estimated, the relative error of the estimation can be controlled below 1.5 percent, which enables the CT reconstruction result from the inpainted measurement f to outperform that from original measurement f_0.

In fact, to accomplish high quality CT reconstruction from less projection measurement or lower X-ray projection dose, this thesis ultimately proposes an algorithm based on alternatively optimize the object image u and the inpainted Radon domain f. It can be proved that the alternating optimization algorithm is convergent. Furthermore, the numerical simulation results indicate that our proposed method performs better than all existing methods in terms of visual quality, relative error and correlation. The details of Radon domain inpainting mechanism will be illustrated and analyzed in Section 3.1.1.

Another problem which cannot be solved by model (1.4) is the robustness to inaccurate projection matrix P caused by the error of beamlet location and direction. To improve the robustness of wavelet frame based CT reconstruction methods, this thesis will apply a three-system method [41, 12] to separate and treat different image parts by different regularization terms. In this thesis, the images will be separated to three different image parts: the information part we want to restore (or cartoon part), the artifacts generated by the error of P, and the noise part. Correspondingly,

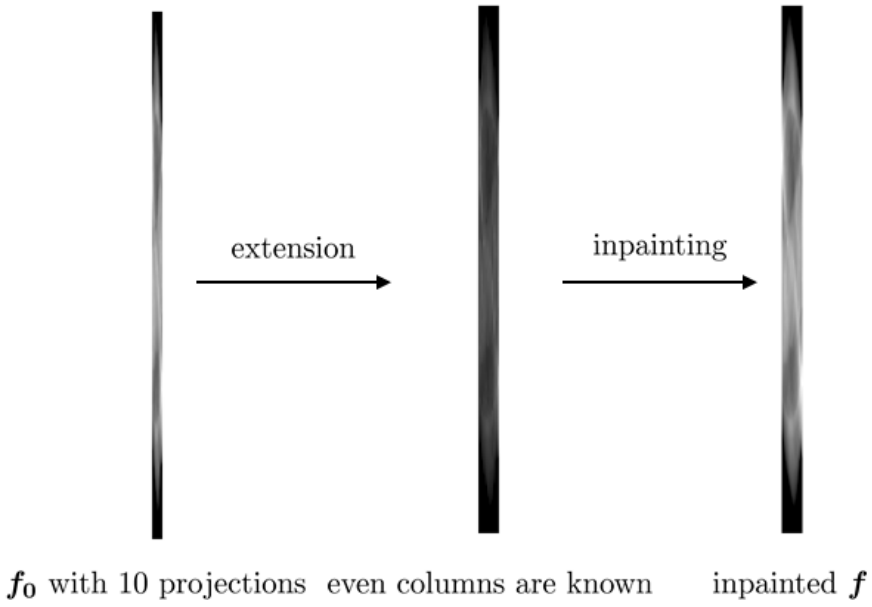

Figure 1.2: The strategy of inpainting in Radon domain.

the three-system model can regularize the noise part with its sparsity in spatial domain, artifacts part in discrete cosine transform (DCT) domain, and information part in wavelet frame transform domain. Moreover, fast and convergent algorithms can easily solve the three-system method to generate each image part. In particular, the information part can be separated from the artifacts and the additive noise. As a result, the three-system method can be robust to the instrument error including the error of P. Since in clinical application, the instrument error is often very huge and can apparently affect the result, the improvement of the robustness can enhance the quality of reconstruction and possibility to further reduce the projection dose. For further research of the multi-system wavelet frame based CT reconstruction methods, readers can refer to Section 3.1.2 of this thesis.

1.2.3 Approximation by B-spline Wavelet System

In this thesis, besides the revision of the approximation of smooth function by B-spline refinable function, a couple of theorems will be generated to show that the B-spline wavelet with vanishing moment l can approximate the l-th order derivatives

of smooth functions. i.e,

$$\|Q_{l,j}f - f\|_p = \|a_l 2^j \sum_{\alpha\in\mathbb{Z}} \langle f, \psi_l(2^j \cdot -\alpha)\rangle \tilde{\phi}(2^j \cdot -\alpha) - D^l f\|_p = O(2^{-nj}) \qquad (1.6)$$

where ψ_l is the B-spline wavelets with vanishing moment l, the function $\tilde{\phi}$ is a designed linear combination of finite shifted B-spline functions. If $\tilde{\phi}$ is simply chosen as the B-spline function ϕ, the approximation order for (1.6) is 2 if the order of the corresponding B-spline is at least 2, i.e, the linear B-spline. With appropriate construction of $\tilde{\phi}$ and sufficient smooth condition of function f, the approximation order n for (1.6) can be arbitrarily high for any fixed low order B-spline wavelet. The method of constructing $\tilde{\phi}$ is also applicable for approximation to the smooth function itself and such method for pursuing higher approximation order is more general than that in [33]. The approximation result (1.6) shows that for a smooth function f which can be regarded as the locally smooth pieces of images, besides the approximation of f itself by low frequency coefficients, the wavelet coefficients can approximate various different order of derivatives (partial derivatives for 2-dimensional case) of f.

Based on the approximation of functions and its derivatives in high approximation order, this thesis also generates several corollaries showing the approximation to the Sobolev norms of smooth functions. The approximation order can be arbitrarily high as well as the approximation of functions and their derivatives.

1.3 Outline of the thesis

The rest of this thesis will be organized as follows. In Chapter 2, we will propose two sparsity-based regularization models for the blind image inpainting problem. The summaries and conclusions for different research topics will be provided at the end of all following chapters. In Chapter 3, we will propose two different techniques for pursuing better quality of CT image reconstruction from low and inaccurate projection dose. For numerical simulations, we will compare our result with most popular methods such as FBP, TV regularized method and some existing wavelet tight frame based methods. In Chapter 4, we want to give the explicit form of the quasi-projection operator for arbitrary high order approximation to any order derivatives of smooth functions.

Chapter 2

Blind Image Inpainting

In solving image inpainting problems, the index set Λ^c of the missing/damaged pixels is usually given or estimated by pre-detectors. With a well estimated or exact value of Λ^c, the image inpainting problem is called the non-blind inpainting problem which can be restored with high quality by wavelet frame based method. In some cases, however, the pixels corrupted by random-valued impulse noise are difficult to be accurately estimated by pre-detectors if the image is also degraded by additive Gaussian noise. As a result, it is necessary to solve the image inpainting problem without priori knowledge of the index set Λ^c of the missing/damaged pixels. Such image inpainting problem is called the blind image inpainting problem. In this chapter, two wavelet frame based blind inpainting models, named the single-system model and the two-system model, will be proposed for treating the random-valued impulse noise without the prior knowledge of Λ^c. In particular, the two-system model can intelligently preserve the textures while removing the scratches in the image. Then, we will introduce the split Bregman algorithm and its specific forms for solving the proposed blind inpainting models. At last, numerical simulations will show that in the image restorations with random-valued impulse noise, the proposed blind inpainting models are comparable or even better than the two-stage inpainting methods with pre-detectors such as the ROLD detector [38].

2.1 Models and Algorithms

In this chapter, for notational convenience, the pixel-wise projection matrix A_Λ associated to Λ is set as an $n \times n$ diagonal matrix with the diagonal entries 1 for the

indices in Λ and 0 for the indices in Λ^c. Under this notation, the image inpainting problem (1.1) can be reinterpreted as

$$A_\Lambda f = A_\Lambda(Hu + \epsilon) \quad \text{and} \quad A_{\Lambda^c} f = A_{\Lambda^c} v. \tag{2.1}$$

By the definition in (2.1), the fidelity information is given by $Hu + v \approx f$. Due to the difficulty of accurate estimation of the index set Λ^c, we assume that the outlier part v is sparse in spatial domain. Consequently, it is reasonable to use the ℓ_1 norm regularization of v in the object function to separate the outlier from the restored images. Combining the term $\|v\|_1$ together with the fidelity term $\frac{1}{2}\|Hu+v-f\|_2^2$ and appropriate regularization term of u in certain domain, the blind inpainting models can be proposed as in the following subsections. The corresponding algorithms will be provided after the definition of the proposed blind inpainting models.

2.1.1 Single-system Model

The single-system blind image inpainting model for (2.1) can be proposed as follows:

$$\min_{u,v} \quad \frac{1}{2}\|Hu + v - f\|_2^2 + \lambda_1\|Wu\|_1 + \lambda_2\|v\|_1, \tag{2.2}$$

where u is the true image for image inpainting problem, v is a random-valued vector in the observed image f, the matrix H is some degradation matrix, and W is a decomposition matrix associated to some tight framelet system. In general, the model (2.2) is designed to recover an image u with sparse representation in the tight frame transform domain, i.e. the coefficients of Wu are sparse; and simultaneously to estimate a sparse random-valued vector v in image domain. As a convex relaxation of ℓ_0-norm regularization, ℓ_1-norm is used on both Wu and v in (2.2) to measure their sparsities in the corresponding domains.

In the proposed model (2.2), the vector v is explicitly regarded as an unknown variable. On the other hand, some alternative approaches are available to handle the random-valued vector v. Two of them appearing in [11, 54] are two-staged approaches that estimates the inpainting region Λ before solving the solution of u. As a result, the two-staged method can reduce (2.1) into a regular inpainting problem:

$$\min_{u} \quad \frac{1}{2}\|A_\Lambda(Hu - f)\|_2^2 + \lambda\|Wu\|_1. \tag{2.3}$$

The two-staged approach (2.3) has good performance with the accurate detection of Λ, *e.g.* the detection of salt-and-pepper noise using adaptive median filter ([14]). However, it is much more difficult to accurately detect general random-valued impulse noise in images. Furthermore, the detection errors of Λ could hamper the quality of the inpainting.

Another approach was first proposed by [3, 4] in the application of image deblurring with impulse noise. The approach can be defined as in (2.4).

$$\min_{u} \quad \|Hu - f\|_1 + \lambda \|Wu\|_1. \tag{2.4}$$

Compared to (2.2), the model (2.4) absorbs the outlier v in the fidelity term $Hu - f$. Therefore, the model (2.4) uses ℓ_1 norm in the fidelity term $Hu - f$ due to sparsity of outlier in the image domain. As a matter of fact, the model (2.4) is also applicable for blind image inpainting problems. In numerical simulations, the model (2.4) has almost the same performance as the proposed model (2.2) if the missing/damaged pixels are purely caused by impulsive noise. In practice, however, image noise is usually from multiple sources. For instance, [52] identified totally five major sources of image noise which have different statistical distributions but frequently occurs simultaneously in many image restoration applications. In the simultaneous presence of multiple types of noise such as the mixed impulse noise and Gaussian noise, the model (2.2) performs better than (2.4), which can be seen in the numerical simulations in the later part of this chapter. The reason of the numerical result can be explained as below. First, our proposed model (2.2) has the ℓ_1 norm regularization of v which can separate the sparse outlier part as well as the ℓ_1 fidelity term in (2.4). What is more, the ℓ_2 norm fidelity term in our model (2.2) can also optimally estimate the pollution of Gaussian noise while the model (2.4) cannot.

2.1.2 Two-system Model

The model (2.2) has good performance for blind inpainting if the true image is piecewise smooth and the outlier has sparse representation in image domain so that the regularization of Wu and v correspond these properties. In some circumstances in practice, the true images may exist rich texture features which are not piecewise smooth but has good sparsity in image domain ([2, 23, 63]). Therefore the model

(2.2) is likely to identify these textures as outlier and save them in the vector v, which lead to the result image u not including these necessary textures.

To preserve the textures while suppressing the outlier, it is necessary to generate another model with one more system to separate the texture out of the outlier part. Since many types of textures, especially the periodical structure of textures, have sparse representation in local discrete cosine transform (LDCT) domain (see the applications in [41, 12, 16]), applying the multi-system method as well as the model (3.4) in Chapter 3, the blind inpainting model with two systems can be proposed as follows:

$$\min_{u_1,u_2,v} \quad \frac{1}{2}\|H(u_1+u_2)+v-f\|_2^2+\lambda_1\|Wu_1\|_1+\lambda_2\|v\|_1+\lambda_3\|Du_2\|_1. \tag{2.5}$$

where the matrix D denotes the LDCT transform, u_1 and u_2 are the cartoon part and texture part of the true image $u = u_1 + u_2$. Compared to the model (2.2) with single system, the two-system model (2.5) has better preservation of texture features but nearly twice time and memory consumption. Therefore, it is better to choose the model (2.2) for inpainting images with less textures to save computational time and memory cost. On the other hand, model (2.5) is more suitable for images with rich textures.

2.1.3 Split Bregman Algorithm

In this subsection, we give a brief introduction of the basic idea of split Bregman algorithm which is applied for the blind inpainting method and all the proposed CT reconstruction methods in Chapter 3. The split Bregman algorithm was initially proposed in [50] and then was shown to be convergent and powerful in [50, 91] when it is applied to various variational models for image restoration, e.g., ROF [69] and nonlocal variational models [47]. Interested readers are referred to [50, 16] for more details of the split Bregman algorithm.

Consider the following minimization problem

$$\min_{u} \quad E(u)+\lambda\|Wu\|_{1,p}, \tag{2.6}$$

where $E(u)$ is a smooth convex functional and W is the wavelet decomposition

operator. Let $d = Wu$ and then (2.6) can be rewritten as

$$\min_{u,d=Wu} \quad E(u) + \lambda \|d\|_{1,p}. \tag{2.7}$$

Note that u and d are two variables connected by the constraint $d = Wu$. The derivation of the split Bregman iteration for solving (2.7) is based on the Bregman distance ([50, 16]). Recent research (see e.g. [42, 82]) showed that the split Bregman algorithm can be derived by applying the augmented Lagrangian method (see e.g. [48]) to (2.7). The connection between the split Bregman algorithm and the Douglas-Rachford splitting was addressed by [75]. Skipping the detailed derivations, we directly state the split Bregman algorithm solving (2.6) through (2.7) as follows

$$\begin{cases} u^{k+1} = \arg\min_u E(u) + \frac{\mu}{2}\|Wu - d^k + b^k\|_2^2, \\ d^{k+1} = \arg\min_d \lambda\|d\|_{1,p} + \frac{\mu}{2}\|d - Wu^{k+1} - b^k\|_2^2, \\ b^{k+1} = b^k + Wu^{k+1} - d^{k+1}. \end{cases} \tag{2.8}$$

By the result from [39, 31], the second step is equivalent to a soft-thresholding operation. Therefore, (2.8) can be rewritten as

$$\begin{cases} u^{k+1} = \arg\min_u E(u) + \frac{\mu}{2}\|Wu - d^k + b^k\|_2^2, \\ d^{k+1} = \mathcal{T}^p_{\lambda/\mu}(Wu^{k+1} + b^k), \\ b^{k+1} = b^k + (Wu^{k+1} - d^{k+1}), \end{cases} \tag{2.9}$$

where $\mathcal{T}_t^p$ is the soft-thresholding operator defined by

$$(\mathcal{T}_t^p(v))_{l,i,j} = \begin{cases} v_{l,i,j}, & \text{if } (i,j) = (0,0) \\ \frac{v_{l,i,j}}{|v_{l,i,j}|}\max(|v_{l,i,j}| - t, 0), & \text{if } (i,j) \neq (0,0), p = 1 \\ \frac{v_{l,i,j}}{R_l}\max(R_l - t, 0), & \text{if } (i,j) \neq (0,0), p = 2 \end{cases} \tag{2.10}$$

with $R_l = (\sum_{(i,j)\neq(0,0)} |v_{l,i,j}|^2)^{\frac{1}{2}}$.

It can be seen that the first step of (2.9) usually involves the procedure of solving linear systems, while the last two steps are relatively straightforward with $O(1)$ complexity.

2.1.4 Blind Inpainting Algorithms

The single-system blind image inpainting model (2.2) can be efficiently solved by the split Bregman algorithm. If we add a new variable $d = Wu$ and rewrite (2.2) as

$$\min_{u,v,d=Wu} \quad \frac{1}{2}\|Hu + v - f\|_2^2 + \lambda_1\|d\|_1 + \lambda_2\|v\|_1.$$

then the model can be solved in an outline shown as below:

$$\begin{cases} u^{k+1} = \arg\min_u \frac{1}{2}\|Hu + v^k - f\|_2^2 + \frac{\mu}{2}\|Wu - d^k + b^k\|_2^2, \\ v^{k+1} = \arg\min_v \lambda_2\|v\|_1 + \frac{1}{2}\|v - (f - Hu^{k+1})\|_2^2, \\ d^{k+1} = \arg\min_d \lambda_1\|d\|_1 + \frac{\mu}{2}\|d - (Wu^{k+1} + b^k)\|_2^2, \\ b^{k+1} = b^k + (Wu^{k+1} - d^{k+1}). \end{cases}$$

The detail of the split Bregman algorithm solving (2.2) is shown in the following Algorithm 1.

Algorithm 1 Numerical algorithm for solving (2.2)

(i) Set initial guesses $u^0 = 0$, $v^0 = 0$, $d^0 = 0$, $b^0 = 0$. Choose an appropriate set of parameters $(\lambda_1, \lambda_2, \mu)$.

(ii) For $k = 0, 1, \ldots$, perform the following iterations until the stopping criteria is $\|d^k - Wu^k\|_2 \leq \epsilon$ is met,

$$\begin{cases} u^{k+1} = (H^\top H + \mu W^\top W)^{-1}\left(H^\top(f - v^k) + \mu W^\top(d^k - b^k)\right), \\ v^{k+1} = \mathcal{T}_{\lambda_2}(f - Hu^{k+1}), \\ d^{k+1} = \mathcal{T}_{\lambda_1/\mu}(Wu^{k+1} + b^k), \\ b^{k+1} = b^k + (Wu^{k+1} - d^{k+1}). \end{cases} \tag{2.11}$$

Note that the linear system in the first equation of (2.11) is positive definite and sparse, thus the linear system can be solved by the conjugate gradient (CG) method. In our numerical simulations, only a few iterations of CG method are executed to approach an approximate solution with the property $\|d^k - Wu^k\|_2 \leq \epsilon$.

Regarding to the two-system model, the corresponding split Bregman algorithm is more complicated but the principle is the same. The details of the algorithm can be generated similarly as in Algorithm 2. As well as in Algorithm 1, CG method is

carried out when solving the linear systems for both u_1 and u_2.

Algorithm 2 Fast algorithm for solving (2.5)

(i) Set initial guesses $u_1^0 = 0$, $u_2^0 = 0$, $v^0 = 0$, $d_1^0 = 0$, $b_1^0 = 0$, $d_2^0 = 0$, $b_2^0 = 0$. Choose an appropriate set of parameters $(\lambda_1, \lambda_2, \lambda_3, \mu_1, \mu_2)$.

(ii) For $k = 0, 1, \ldots$, perform the following iterations until the stopping criteria $\|{d_1}^k - W{u_1}^k\|_2 + \|{d_2}^k - D{u_2}^k\|_2 \leq \epsilon$ is met

$$\begin{cases} {u_1}^{k+1} = (H^\top H + \mu_1 W^\top W)^{-1} \left(H^\top (f - H u_2^k - v^k) + \mu_1 W^\top (d_1^k - b_1^k) \right), \\ {u_2}^{k+1} = (H^\top H + \mu_2 D^\top D)^{-1} \left(H^\top (f - H u_1^{k+1} - v^k) + \mu_2 D^\top (d_2^k - b_2^k) \right), \\ v^{k+1} = \mathcal{T}_{\lambda_2}(f - H({u_1}^{k+1} + {u_2}^{k+1})), \\ d_1^{k+1} = \mathcal{T}_{\lambda_1/\mu_1}(W{u_1}^{k+1} + b_1^k), \\ b_1^{k+1} = b_1^k + (W{u_1}^{k+1} - d_1^{k+1}), \\ d_2^{k+1} = \mathcal{T}_{\lambda_3/\mu_2}(D{u_2}^{k+1} + b_2^k), \\ b_2^{k+1} = b_2^k + (D{u_2}^{k+1} - d_2^{k+1}). \end{cases}$$

2.2 Numerical Results

In this section, the general image degradation model including the possible impulse and Gaussian noise pollution can be defined as follows:

$$f = N_p(Hu + \epsilon),$$

where u is the ground truth image before corruption, f represents the corrupted image. H is the blurring operation matrix which is uniquely determined by the blur kernel, or identical matrix if the image is not blurred, ϵ denotes the i.i.d. Gaussian white noise with zero mean. The operator N_p for adding impulse noise can be defined as follows:

Impulsive noise: a certain proportion of pixels (chosen randomly) are altered to be an unknown value satisfies a certain probability distribution.

$$N_p(x_{ij}) = \begin{cases} d_{ij}, & \text{with probability } r, \\ x_{ij}, & \text{with probability } (1 - r), \end{cases}$$

where $r \in [0, 1]$ the level of random valued noise. If the N_p specially stands for adding random-valued impulse noise, d_{ij} becomes a uniformly distribution random number in $[d_{min},\ d_{max}]$. In this chapter, the dynamic range $[d_{min},\ d_{max}]$ is always set as $[0, 255]$.

In the following numerical simulations, the peak signal to noise ratio (PSNR) measurement is used for quantitative evaluation of the restoration results. The PSNR value is defined as follows:

$$\mathrm{PSNR}(\widehat{x}, x) = 10 \log_{10} \frac{255^2}{\frac{1}{mn} \sum_{i=1}^{m} \sum_{j=1}^{n} (\widehat{x}_{ij} - x_{ij})^2},$$

where m and n describe a size of the image, x_{ij} is the intensity value of the ground truth image at the pixel location (i, j), and $\widehat{x}_{ij}$ represents the intensity value of the restored image at location (i, j).

Through the numerical experiments, 100 iterations are executed in both Algorithm 1, Algorithm 2 when solving the proposed single-system and two-system models. Regarding to the numerical simulations, running the MATLAB code of the proposed models requires approximately $60 \sim 120$ seconds using a PC with 2GHz Intel Core 2 CPU. The time and memory consumption on the other compared methods is at the same level as the proposed frame based blind inpainting models.

2.2.1 Removing Random-valued Impulse Noise

In practice, besides the Gaussian white noise which is most frequently seen, the impulse noise also exists in many degraded images caused by transmission errors, faulty sensors and etc. Generally, the impulse noise mainly contains two different types, the salt-and-pepper noise and the random-valued impulse noise. Since the pixels corrupted by the impulse noise contain no information of the true image, removing impulse noise is essentially an image inpainting problem. The pixels corrupted by salt-and-pepper noise have intensity value either 0 or 255. Therefore, the index set of damaged pixels can be accurately identified by the adaptive median filter (AMF) (see *e.g.* [29, 53, 15]). However, the random-valued impulse noise is much more difficult to be accurately detected because of its undetermined intensity value. The adaptive center-weighted median filter (ACWMF) [29] and ROLD detection methods [38] are two possible method to roughly estimate the index set of the damaged pixels where the latter one has relatively higher accuracy. The existing

two-stage method is the combination of one noise detection method and the reconstruction model (2.3). On the contrary, the blind inpainting models do not need the priori knowledge of the index set of the missing/damaged pixels from the given information or a detection pre-process.

This paragraph is devoted to the description of the parameter settings. In the single-system model (2.2), the parameter $\lambda_1 \in \{1.8, 2, 2.2, 3\}$ and $\lambda_2 \in \{5, 6\}$ are determined by the Gaussian noise level and the impulse noise level, respectively. In the two-system model (2.5) , the parameters λ_1 and λ_2 is the same as the single-system model (2.2). The parameter λ_3 in model (2.5) is either 1 or 5 determined by the amount of texture features in the true images.

The visual quality of some restored images are shown in Figure 2.1 and Figure 2.2. The PSNR values of all six methods can be seen in Table 2.1 and 2.2. The above figures and tables show clearly that the ROLD detector outperforms the ACWMF detector for images corrupted by random-valued impulse noise. However, even if for the ROLD detector, the detection accuracy can apparently fall down if the random-valued impulse noise is mixed with Gaussian white noise. As is seen in the above figures and tables, the proposed blind inpainting models (2.2) and (2.5) outperform the compared models (2.4) and (2.3) in terms of both the visual quality and PSNR values, especially when the noise level of impulse noise is 10%. When the proportion of damaged pixels increases, the sparsity of v decreases which reduce the performance of the proposed blind inpainting models. However,when the impulse noise level is 20% or 40%, our proposed blind inpainting models can still generally outperform the two-stage methods in terms of identifying the outlier v and restoring the image u, especially for the cases of corruption by mixed Gaussian noise and random-valued impulse noise.

It should be admitted that the proposed blind inpainting models are not applicable for recovering image with more than 50% of pixels missing or damaged by impulse noise. The reason can be explained as the automatic separation of outlier v and piecewise smooth image u requires the sparse representation in corresponding domains but the sparsity dose not exist if too many pixels are corrupted and irrelevant to the ground truth image u. One better alternative method is to apply a two-stage method which first detects the index set of pixels corrupted by random-valued impulse noise (e.g, ACWMF or ROLD method) and then uses model (2.3) to remove the impulse noise and estimate the true images.

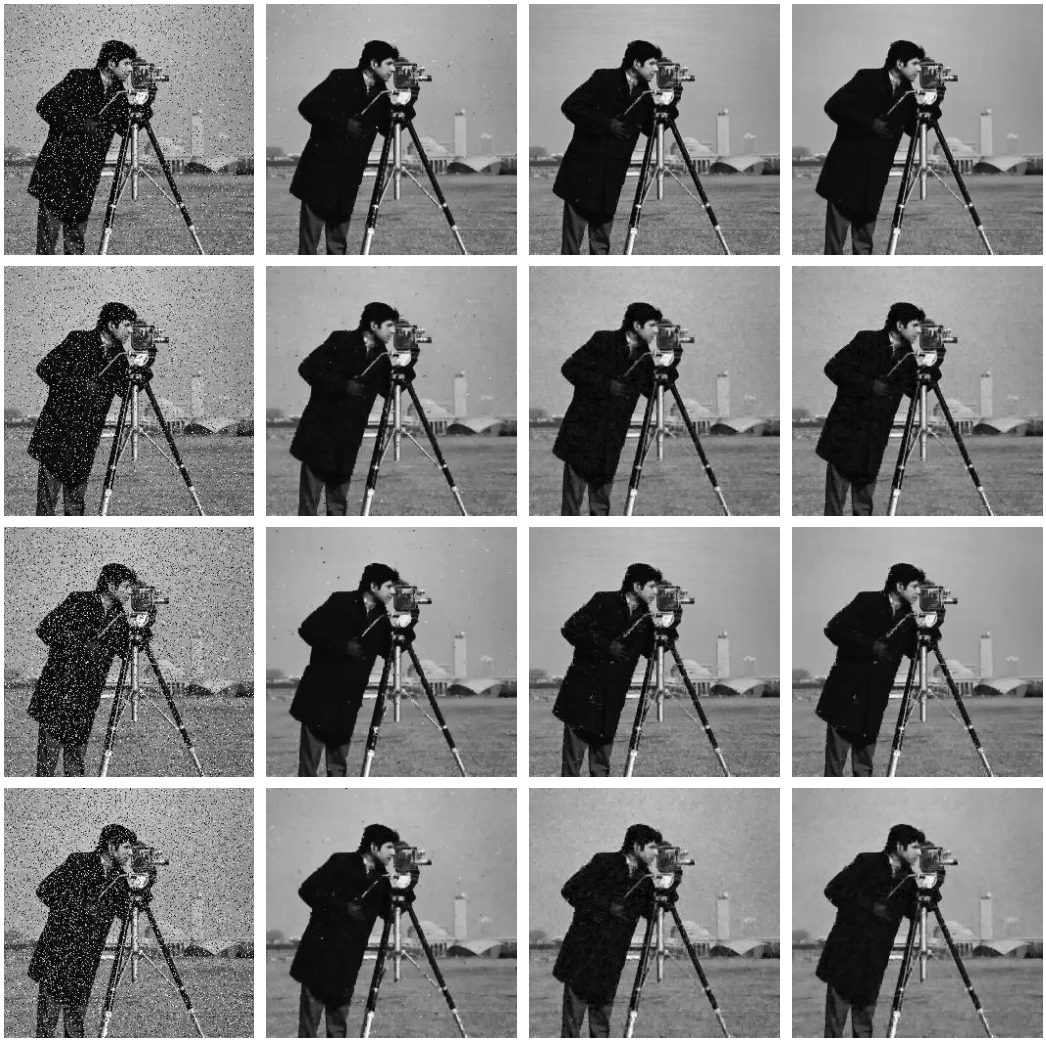

Figure 2.1: Denoising results of cameraman image contaminated by both random-valued impulse noise and Gaussian noise. Images in each column represent (from left to right) corrupted images, results from (2.3) combined with ROLD pre-detection, results from (2.4) and results from (2.2) respectively. The noise levels of corrupted images (from top to bottom) are as follows. (1) 10% random-valued impulse noise without Gaussian noise; (2) 10% random-valued impulse noise with Gaussian noise of σ=10; (3) 20% random-valued impulse noise without Gaussian noise (4) 20% random-valued impulse noise with Gaussian noise of $\sigma = 10$. The PSNR values of the results are given in Table 2.1.

Figure 2.2: Denoising result of several images contaminated by random-valued impulse noise of rate 10% and Gaussian noise of σ=10. Images in each column represent (from left to right) corrupted images, results from (2.3) combined with ROLD predetection, results from (2.4) and results from (2.2) respectively. The PSNR values of the results are given in Table 2.2.

Table 2.1: PSNR value (dB) of the denoising results for cameraman image from all the three models from (2.3), (2.4) and (2.2) (our model 1), in the presence of random-valued impulse noise with ratio r and Gaussian noise with std σ.

Ratio r and	r = 10%		r = 20%		r = 40%	
standard deviation	σ=0	σ=10	σ=0	σ=10	σ=0	σ=10
ROLD-ERR Model in [38]	27.4	24.6	25.4	23.6	23.6	22.3
Model (2.3) + ACWMF	28.5	26.0	26.3	24.9	23.1	22.5
Model (2.3) + ROLD	28.4	27.5	26.3	25.8	23.7	23.3
Model (2.4)	29.9	27.5	27.1	26.0	23.1	22.9
Model (2.2)	30.3	28.4	27.4	26.6	23.6	23.3
Model (2.5)	30.3	28.4	27.4	26.6	23.6	23.3

Table 2.2: PSNR value (dB) of the denoising results for other images from all the three models from (2.3), (2.4), (2.2) and (2.5), in the presence of random-valued impulse noise with ratio r and Gaussian noise with std=10.

Image and r and	Baboon		Boat		Bridge		Barbara512	
ratio	10%	20%	10%	20%	10%	20%	10%	20%
ROLD-ERR Model in [38]	23.0	21.6	24.7	23.8	23.3	22.1	25.3	23.9
Model (2.3) + ACWMF	23.3	22.2	26.6	25.1	24.2	22.9	26.0	24.6
Model (2.3) + ROLD	24.8	22.9	28.2	26.4	25.3	23.7	27.8	25.8
Model from (2.4)	24.5	23.2	27.6	26.1	25.0	23.4	27.0	25.5
Model from (2.2)	25.1	23.5	28.3	26.4	25.4	23.7	27.9	26.0
Model from (2.5)	25.2	23.5	28.2	26.4	25.4	23.7	27.9	26.0

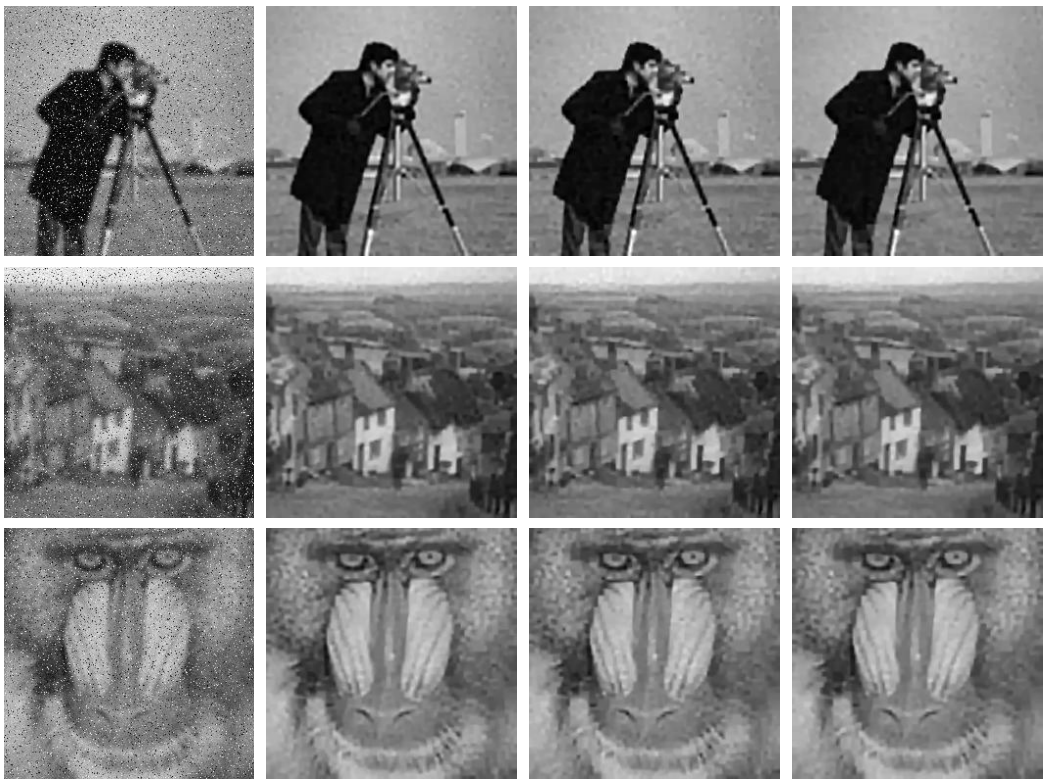

Figure 2.3: Deblurring result of several images in the presence of random-valued impulse noise of rate 10% and Gaussian noise of σ=10. Images in each column represent (from left to right) corrupted images, results from (2.3) combined with ROLD pre-detection, results from (2.4) and results from (2.2). The PSNR values of the results are given in Table 2.3.

2.2.2 Image Deblurring in Presence of Impulse Noise

The proposed blind inpainting algorithm is also applicable for the blurry image corrupted by mixed Gaussian and random-valued impulse noise. The blurring matrix H is equivalent to a 2D convolution with the blur kernel. In this subsection, the blur kernel is chosen as the out-of-focus kernel of radius 6 pixels. The parameters λ_1, λ_2 for both proposed blind inpainting models (2.2) and (2.5) are chosen from the set $\{1, 10, 12\}$. Table 2.3 and Figure 2.3 show that the restored images from all five different methods are more or less the same. In other words, the proposed models (2.2) and (2.5) are comparable to the other three existing models.

Table 2.3: PSNR value (dB) of the results from (2.3), (2.4), (2.2) and (2.5), for image deblurring in the presence of random-valued impulse noise and Gaussian noise.

Image and r and ratio	Cameraman		Goldhill		Baboon	
	10%	20%	10%	20%	10%	20%
Model (2.3) + ACWMF	24.3	24.0	25.7	21.5	21.2	21.2
Model (2.3) + ROLD	24.3	24.1	25.8	21.6	21.3	21.2
Model (2.4)	24.1	23.9	25.5	21.2	21.2	21.1
Model (2.2)	24.2	24.0	25.7	21.4	21.2	21.1
Model (2.5)	24.2	24.0	25.7	21,4	21.3	21.2

2.2.3 Blind Inpainting from Multiple Degradations

Sometimes in practice, the images may be corrupted by simultaneous random-valued impulse noise and scratches without knowing its intensity value beforehand. Therefore, the index set of damaged pixels includes some discrete pixels corrupted by impulse noise and some continuous pixels damaged by scratches. In this subsection, the numerical simulations are related to the image restoration from degradation by these multiple factors. For both the proposed models (2.2) and (2.5), the parameters are always set to be $\lambda_1 = 3.5, \lambda_2 = 5$. Additionally, the parameter λ_3 in (2.5), which is related to the regularization in LDCT transform domain, is either 1/2 or 1 determined by the amount of textures in the true image.

In this subsection, the proposed blind inpainting models (2.2), and (2.5) are compared with the two-stage method (2.3) with ROLD detection as pre-process. From the PSNR values shown in Table 2.4 and the visual results indicated in Figure 2.4, it can be clearly observed that the two-system model (2.5) outperforms the other two models especially for the images "Barbara512" and "Goldhill" with rich textures.

Regarding to the other two models, for the images "Goldhill" and "Cameraman" which have fewer textures, the single-system model (2.2) outperformed the two-stage model (2.3) with ROLD detector. However, for the image "Barbara512" which has relatively more textures, the two-stage model (2.3) with ROLD detector has better performance compared to the proposed single-system model. The reason for the above result can be explained as follows. On one hand, the image restoration quality of the two-stage method is directly determined by the accuracy of ROLD detector which can be strongly disturbed by thick scratches or additive Gaussian noise. Therefore, the advantage of single-system model (2.2) would dominate the

Figure 2.4: The blind inpainting results for images damaged by both impulse noise, scratch and Gaussian noise with std=10. Three sample images are shown (from top to bottom): "Barbara", "goldhill" and "cameraman". Images in each column represent (from left to right) corrupted image, restored image by (2.3) with ROLD pre-detector, restored image by (2.2) and restored image by (2.5). The PSNR values of the results are given in Table 2.4.

result if there is less textures. On the other hand, the disadvantage of the single-system model (2.2) for the image "Barbara512" is caused by misidentification of the texture features together with the scratch as the outlier v. As an advanced version of (2.2), the two-system model (2.5) can separate the texture features into the LDCT system and preserve them in the restored image. Therefore, the preservation of textures and better treatment with Gaussian white noise and random-valued impulse noise leads to the best performance of two-system blind inpainting model (2.5) among all three methods.

Table 2.4: PSNR value (dB) of the results for inpainting experiments on images degraded by mixed factors, where the rate of random-valued impulse noise is set as 10%.

Image	Standard deviation σ of Gaussian noise	(2.3) with ROLD	(2.2)	(2.5)
Barbara512	0	25.2	24.6	25.2
	10	24.7	24.3	24.7
Goldhill	0	25.6	26.5	27.2
	10	24.4	26.0	26.4
Cameraman	0	23.4	24.8	24.9
	10	23.3	24.5	24.6

2.3 Summary

This chapter focused on the blind image inpainting problem without knowing the index set of missing/damaged pixel from given information or pre-detection. Two wavelet frame based models and their corresponding fast algorithms have been proposed for solving the blind inpainting problems. The models are generated based on the sparsity of cartoon part in the wavelet transform domain and the sparsity of the outlier part in image domain. Based on the split Bregman algorithm, the different variables in the minimization problem can be alternatively optimized to approach their optimal solutions. The numerical simulations show that compared to the two-stage methods with pre-detection, the proposed blind inpainting models perform equally or even better in the image restoration from damage by random-valued impulse noise with possible Gaussian noise, blurring effect, or scratches. Moreover, Subsection 4.2.3 shows that the proposed two-system method has special advantage in protecting the textures when suppressing the noise and scratches. The numerical results give an alternative way to restore or inpaint the images besides the existing methods which mainly rely on the given index set of missing/damaged pixels or the accuracy of the relative pre-detectors. For some cases such as removing random-valued impulse noise with noise level less than 50%, the blind inpainting scheme can generate an even better restoration result. However, the blind inpainting models are still not robust to some types of noise such as the Poisson noise. In future, the research of blind inpainting models should be focused on its robustness to more different types of mixed noise or other sorts of image degradations. Another possible direction of improvement is based on pursuing a better identification of outliers v so that the quality of removing random-valued impulse noise can be improved from

the current level.

Chapter 3

CT Image Reconstruction from Low Dose

In the clinical applications of X-ray Computed Tomography (CT), it is important to reduce the X-ray dose while maintaining the quality of CT image reconstruction. The widely used filtered back-projection (FBP) method [44, 35, 64, 60] and the algebraic reconstruction technique (ART) method [51] cannot reconstruct a clear image if the amount of measurement data is less than half of the anticipated image resolution. The total variation (TV) regularized method [59] and the anisotropic wavelet frame based method [58] have made a huge progress in preserving the quality of reconstruction with reduced measurement.

In this chapter, we will propose two reinforced wavelet frame based methods to further improve the quality of CT image reconstruction from even less amount of measurement. First, the isotropic wavelet frame regularization, which treats the singularities in different directions equally, is introduced to all the proposed models. Then, the Radon domain inpainting mechanism is introduced to improve the reconstruction quality if the amount of measurement is highly insufficient. Moreover, the multi-system method is proposed to treat with the artifacts generated by the mechanical error of the projection matrix P. The alternating algorithms based on the split Bregman algorithm will be proved to be convergent. The numerical simulations clearly showed the advantage of the isotropic wavelet frame regularization and the Radon domain inpainting mechanism in terms of visual quality and numerical evaluation. The numerical results also indicated that for the reconstruction of both simulated phantom and the preclinical sheep lung, the multi-system method outperforms the popular FBP and SART+TV methods in terms of relative error, correlation, the contrast-to-noise ratio (CNR), and the mean structural similarity

[90]. At last, this chapter showed that the proposed multi-system method is also applicable to interior tomography.

3.1 Frame Based Models

This section is devoted to the proposition of two wavelet frame based CT image reconstruction models. Both models applied the isotropic wavelet frame regularization term which can be defined by (3.2) with $p = 2$. Since the artifacts generated during CT image reconstruction do not necessarily have the vertical or horizontal direction, the isotropic wavelet frame regularization should have better effect in removing the artifacts and preserving the edges and features. The two proposed models applied the Radon domain inpainting mechanism and the multi-system regularization scheme, respectively. The details and the purposes of the proposed CT image reconstruction models are shown in the following subsections.

3.1.1 Radon Domain Inpainting Model

In this subsection, we denote f_0 as the observed measurement defined on grid Λ of size $N_m \times N_p$ where N_m is the number of sample points on the X-ray detector and N_p is the number of projections for acquiring f_0. Denote the higher resolution projected image as f defined on the grid $\Omega \supset \Lambda$. From a practical concern, we will only consider inpainting with respect to projection angles (see Figure 1.1 in Chapter 1). As a result, by our configuration, Ω will become an $N_m \times 2N_p$ grid whose even columns are the columns of Λ. Therefore, the number of projections for the operator P that corresponds to f is $2N_p$. If we define the restriction operator R_Λ as $(R_\Lambda v)[i, j] := v[i, j]$ for $(i, j) \in \Lambda$ and zero elsewhere, the constraint of f should satisfy $R_\Lambda f = f_0$, meaning the inpainted high resolution measurement should be consistent within the region of the observed measurement f_0. In our model, however, we would not enforce such constraint to be exactly satisfied since f_0 is likely to contain noise. We note that besides R_Λ, some other similar operators for preserving the data consistency have also been proposed in e.g. [66, 87].

The isotropic wavelet tight frame regularized CT image reconstruction model

using Radon domain inpainting mechanism can be stated as follows:

$$\begin{aligned}\min_{f,u}\ \frac{1}{2}\|R_{(\Omega\setminus\Lambda)}(Pu-f)\|_2^2+\lambda_1\|W_1 f\|_{1,p}+\lambda_2\|W_2 u\|_{1,p}\\ +\frac{\kappa}{2}\|R_\Lambda f-f_0\|_2^2+\frac{1}{2}\|R_\Lambda(Pu)-f_0\|_2^2,\end{aligned}\tag{3.1}$$

where the last term has the same weights $\frac{1}{2}$ as the first term since they both represent the fidelity in Radon domain. The norm $\|\cdot\|_{1,p}$ can be defined as

$$\|Wu\|_{1,p}=\left\|\sum_{l=1}^{L}\Big(\sum_{(i,j)\neq(0,0)}|W_{l,i,j}u|^p\Big)^{\frac{1}{p}}\right\|_1,\quad p=1,2.\tag{3.2}$$

In the equation (3.2), when $p=1$, the norm $\|\cdot\|_{1,1}$ is called as the *anisotropic* ℓ_1-norm of the wavelet tight frame coefficients, which is the standard ℓ_1-norm used for majority of wavelet frame based image restoration problems. When $p=2$, the norm $\|\cdot\|_{1,2}$ is called as the *isotropic* ℓ_1-norm of the wavelet tight frame coefficients, which was first proposed in [13]. It was shown [13] that for some image restoration problems, isotropic ℓ_1-norm outperforms anisotropic ℓ_1-norm for analysis based approach in terms of both visual quality of the restored images and efficiency of the corresponding numerical algorithm. In this thesis, it will be shown in Section 3.3 that for the CT image reconstruction problem, isotropic ℓ_1-norm also performs better than anisotropic ℓ_1-norm.

In our proposed model (3.1), both the first term $\frac{1}{2}\|R_{(\Omega\setminus\Lambda)}(Pu-f)\|_2^2$ and the last term $\frac{1}{2}\|R_\Lambda(Pu)-f_0\|_2^2$ serve as the data fidelity terms. The simpler fidelity term $\frac{1}{2}\|(Pu-f)\|_2^2$ is not used because f is the estimated projection data which is generally not as reliable as f_0. As a result, in the domain Λ where the actual measurement f_0 is available, we should guarantee that $Pu\approx f_0$ on Λ. The term $\frac{1}{2}\|R_\Lambda f-f_0\|_2^2$ makes sure that the recovered higher resolution projected image f is consistent with f_0 on Λ. The terms $\lambda_1\|W_1u\|_{1,p}$ and $\lambda_2\|W_2f\|_{1,p}$ are regularization terms which lead the reconstructed images u and f to be piecewise smooth. The operator W_1 denotes the cubic B-spline framelet transform with 3 levels of decomposition, and the operator W_2 represents the linear B-spline framelet transform with 1 level of decomposition.

In fact, the model (3.1) is general and includes the analysis based approach for CT reconstruction without Radon domain inpainting as a special case. If we let

$\Omega = \Lambda$ and $\kappa = \infty$, the model (3.1) can be equivalently reinterpreted as

$$\min_u \quad \frac{1}{2}\|Pu - f\|_2^2 + \lambda\|Wu\|_{1,p}, \tag{3.3}$$

where the operator W is equivalent to W_2 in (3.1). When $p = 1$ in (3.3), model (3.3) is the general analysis based approach [16, 41, 81]. In fact, the model (3.3) is the duplication of (1.4). In the rest of this chapter, we shall refer to model (3.3) with $p = 1$ as the anisotropic wavelet frame based model; and refer to model (3.3) with $p = 2$ as the isotropic wavelet frame based model.

3.1.2 Multi-system Models

In this subsection, we propose another analysis based approach which is robust for inaccurate estimation of projection matrix P. The robustness comes from the application of a three-system method [41, 12] to separate and treat different image parts by different regularization terms. In this thesis, the images can be separated to three different image parts: the cartoon part we want to restore, the artifacts part generated by the error of P, and the noise part. The three-system model can regularize the noise part with its sparsity in Radon domain, artifacts part in discrete cosine transform (DCT) domain, and information part in wavelet frame transform domain. Such an idea was initially implemented in robust image deblurring with inaccurate blur kernels ([55]), in which the inaccurate blur kernel is essentially the error of the linear operator from the image to its corresponding measurement. Therefore, in this paper the error of P is similar as the error of blur kernels. The robust analysis based approach model is as:

$$\min_{u,a,n} \quad \frac{1}{2}\|P(u+a) + n - f\|_2^2 + \lambda_1\|Wu\|_{1,2} + \lambda_2\|Da\|_1 + \lambda_3\|n\|_1, \tag{3.4}$$

where u is the reconstructed image, a represents the estimated artifacts caused by inaccurate P, and n stands for the additive noise in Radon domain. P is the projection matrix for the special method including totally N_p projections. The matrix $W = \{W_{l,i,j} : 1 \le l \le L, (i,j) \in \{0,1,2\} \times \{0,1,2\}\}$ is the 2D decomposition operator associated with the linear B-spline framelet system. For the wavelet systems, l represents the layer and i, j represent the different windows of the frame coefficient, where only $(i,j) = (0,0)$ stands for the lower-pass coefficient. The operator

D represents the DCT transform. We assume the vector Da is sparse in the corresponding DCT transform domain and the noise vector n is itself sparse in image domain. Since the model (3.4) is convex for all its variables u, a and n, it can be alternatingly optimized to simultaneously converge to the optimized solution by [83, Theorem 4.1]. In particular, the value of u is the true image and the value a and n should be discarded ultimately.

Finally we want to note that regarding the interior tomography, the projection lines in each projection angle would be truncated with the middle part. Therefore, it essentially reduces the rows of the linear system $Pu = f$ and the corresponding model can be generated as well as (3.4) with different P with fewer rows and f with shorter vector length.

3.2 Algorithms

Both proposed CT image reconstruction models (3.1) and (3.4) can be solved through the alternating optimization algorithm. Each step of the alternating optimization algorithm can be generated from the split Bregman algorithm as well as the blind inpainting algorithms. This section is devoted to provide the outline and the details for solving all the proposed models. The convergence analysis of the algorithms are also given in the last part of this section.

3.2.1 Alternating Algorithms

To solve the model (3.1) with Radon domain inpainting mechanism, an alternating optimization algorithm is proposed as in Algorithm 3. Generally the convergence of the alternating algorithm can be proved from [83, Theorem 4.1]. Since both the variables u and f are convex in (3.1), the convergence of Algorithm 3 can be proved although each step in Algorithm 3 provides an approximate solution. The details of the proof is given in Subsection 3.2.2.

Using the split Bregman algorithm (2.8), Step 1 of Algorithm 3 can be solved as

Algorithm 3 Wavelet Frame Based CT Image Reconstruction with Radon domain inpainting mechanism

Step 0. Solve model (3.3) to obtain an initial reconstruction u^0.
while stopping criteria is not met **do**
Step 1. Solve

$$f^{k+1} := \arg\min_f \ \frac{1}{2}\|R_{(\Omega\setminus\Lambda)}(Pu^k - f)\|_2^2 + \lambda_1\|W_1 f\|_{1,p} + \frac{\kappa}{2}\|R_\Lambda f - f_0\|_2^2.$$

Step 2. Solve

$$u^{k+1} := \arg\min_u \ \frac{1}{2}\|R_{(\Omega\setminus\Lambda)}(Pu - f^{k+1})\|_2^2 + \lambda_2\|W_2 u\|_{1,p} + \frac{1}{2}\|R_\Lambda(Pu) - f_0\|_2^2.$$

end while

follows:

$$\begin{cases} f^{k+1} := (R_{(\Omega\setminus\Lambda)} + \mu_1 I + \kappa R_\Lambda)^{-1}(R_{(\Omega\setminus\Lambda)}(Pu^k) + \mu_1 W_1^\top(d_1^k - b_1^k) + \kappa R_\Lambda f_0), \\ d_1^{k+1} := \mathcal{T}^p_{\lambda_1/\mu_1}(W_1 f^{k+1} + b_1^k), \\ b_1^{k+1} := b_1^k + (W_1 f^{k+1} - d_1^{k+1}). \end{cases} \tag{3.5}$$

If $\kappa = 1$, in the first equation we have $R_{(\Omega\setminus\Lambda)} + R_\Lambda = I$. The stopping criteria is posed as $\|d_1^k - W_1 u^k\| \le \epsilon_f$ with ϵ_f being a given tolerance. Conjugate gradient method is used to solve the linear system in the first step of (3.5).

The algorithms for Step 0 and Step 2 of Algorithm 3 are almost the same except the operator P corresponds to different number of projections and $\Omega = \Lambda$ for Step 0. The algorithms can be summarized as follows:

$$\begin{cases} u^{k+1} := (P^\top P + \mu_2 I)^{-1}(P^\top(R_{(\Omega\setminus\Lambda)f} + f_0) + \mu_2 W_2^\top(d_2^k - b_2^k)), \\ d_2^{k+1} := \mathcal{T}^p_{\lambda_2/\mu_2}(W_2 u^{k+1} + b_2^k), \\ b_2^{k+1} := b_2^k + (W_2 u^{k+1} - d_2^{k+1}). \end{cases}$$

Similar as (3.5) the stopping criteria is posed as $\|d_2^k - W_2 u^k\| \le \epsilon_u$ where ϵ_u is a given tolerance. The linear system in the first step can be solved by conjugate gradient method.

The multi-system wavelet frame based CT reconstruction model (3.4) can also be solved by a similar alternating optimization algorithm whose outline is summarized in Algorithm 4 with variable ϵ being error tolerance. The convergence of the

alternating optimization scheme can be similarly proved in Subsection 3.2.2.

Algorithm 4 Outline of the alternating optimization algorithm to solve (3.4)

Step 0. Set the initial values such that $u^{-1} = -1, u^0 = 0, a^0 = 0, n^0 = 0, k = 0$.
while stopping criteria ($k \geq 1$ **and** $\|u^k - u^{k-1}\|_2^2 \leq \epsilon$) are not met **do**
Step 1. Solve

$$u^{k+1} := \min_u \quad \frac{1}{2}\|P(u + a^k) + n^k - f\|_2^2 + \lambda_1 \|Wu\|_{1,2}.$$

Step 2. Solve

$$a^{k+1} := \min_a \quad \frac{1}{2}\|P(u^{k+1} + a) + n^k - f\|_2^2 + \lambda_2 \|Da\|_1.$$

Step 3. Solve

$$n^{k+1} := \min_n \quad \frac{1}{2}\|P(u^{k+1} + a^{k+1}) + n - f\|_2^2 + \lambda_3 \|n\|_1.$$

Step 4. Let

$$k := k + 1.$$

end while

The Step 3 in Algorithm 4 can be easily solved by a simple one-time soft thresholding operation as $n^{k+1} := \mathcal{T}^1_{\lambda_3}(f - P(u^{k+1} + a^{k+1}))$. Applying the split Bregman algorithm (2.8), the steps 1 and 2 can be solved fast and accurately. A detailed algorithm to solve (3.4) is summarized in Algorithm 5. Note that the corresponding algorithm for interior tomography is the same as Algorithm 5 except the truncation of P and f.

3.2.2 Convergence Analysis

The alternating optimization methods, sometimes also called the coordinate descent methods, have already become a popular method to solve optimization problems with multiple variables. Based on the convexity condition of all the variables, the convergence analysis has been well-studied in [8, 45, 61, 83, 84]. If the optimization of each variable generates the precise solution, applying [83, Theorem 4.1] can bring out the convergence of the alternating optimization method. In Algorithm 3, the optimization of each variable is direct application of the split Bregman algorithm whose convergence has been proved by [16, 46, 40]. In actual numerical simulation,

Algorithm 5 Detailed Algorithm 4

Step 0. Set the initial values such that $u^0 = u^{-1} = 0, d_u^0 = 0, b_u^0 = 0, a^0 = 0, d_a^0 = 0, b_a^0 = 0, n^0 = 0, k = 0$.

Step 1. Perform the following iterations until the stopping criteria ($k \geq 1$ **and** $\|u^k - u^{k-1}\|_2^2 \leq \epsilon$) are met.

$$
\begin{cases}
u^{k+1} := \arg\min_u \frac{1}{2}\|P(u + a^k) + n^k - f\|_2^2 + \frac{\mu_1}{2}\|Wu - d_u^k + b_u^k\|_2^2 \\
\qquad = (P^\top P + \mu_1 W^\top W)^{-1}(P^\top(f - Pa^k - n^k) + \mu_1 W^\top(d_u^k - b_u^k)) \\
d_u^{k+1} := \mathcal{T}^2_{\lambda_1/\mu_1}(Wu^{k+1} - b_u^k) \\
b_u^{k+1} := b_u^k + (Wu^{k+1} - d_u^{k+1}) \\
a^{k+1} := \arg\min_a \frac{1}{2}\|P(u^{k+1} + a) + n^k - f\|_2^2 + \frac{\mu_2}{2}\|Da - d_a^k + b_a^k\|_2^2 \\
\qquad = (P^\top P + \mu_2 D^\top D)^{-1}(P^\top(f - Pu^{k+1} - n^k) + \mu_2 D^\top(d_a^k - b_a^k)) \\
d_a^{k+1} := \mathcal{T}^1_{\lambda_2/\mu_2}(Da^{k+1} - b_a^k) \\
b_a^{k+1} := b_a^k + (Da^{k+1} - d_a^{k+1}) \\
n^{k+1} := \mathcal{T}^1_{\lambda_3}(f - P(u^{k+1} + a^{k+1}))
\end{cases}
$$

where μ_1 and μ_2 are parameters which do not need to be rigorously chosen since the value will not affect the optimal solution of the model and the convergence of the algorithm. The thresholding operator $\mathcal{T}_t^p$ is defined by (2.10). Note that $W^\top W = I$ and $D^\top D = I$ always hold. The conjugate gradient method can be used to solve the above linear systems when solving u^{k+1} and a^{k+1} in each iteration.

however, Algorithm 1 cannot find the precise solution for each subproblem because only finite iterations can be taken for the split Bregman algorithm and the error always exists. Therefore, strictly speaking, [83, Theorem 4.1] is not applicable to directly show the convergence of Algorithm 3. In this subsection, we will provide a proof which can also be seen in [36] to show that the sequence $\{(u^k, f^k)\}_k$ is bounded and any cluster point of $\{(u^k, f^k)\}_k$ is a solution to (3.1) given the fast decay of error with respect to k.

Let $F(u, f) : \mathcal{R}^n \times \mathcal{R}^m \mapsto \mathcal{R}$ be the objective function of (3.1), i.e.

$$\begin{aligned} F(u,f) = \frac{1}{2}\|R_{(\Omega\setminus\Lambda)}(Pu-f)\|_2^2 + \lambda_1\|W_1 f\|_{1,p} + \lambda_2\|W_2 u\|_{1,p} \\ + \frac{\kappa}{2}\|R_\Lambda f - f_0\|_2^2 + \frac{1}{2}\|R_\Lambda(Pu) - f_0\|_2^2. \end{aligned} \tag{3.6}$$

By the definition of the model, the parameters λ_1, λ_2 and κ are positive constants. It can be easily observed that $F(u, f)$ is a convex and continuous function with respect to both variables u and f. The vector $(\bar{u}, \bar{f})$ is defined as a coordinatewise minimizer of $F(u, f)$ if

$$F(\bar{u},\bar{f}) \le F(\bar{u}+v_u,\bar{f}) \quad \text{and} \quad F(\bar{u},\bar{f}) \le F(\bar{u},\bar{f}+v_f) \quad \forall v_u \in \mathcal{R}^n, \forall v_f \in \mathcal{R}^m.$$

In general, a coordinatewise minimizer is not necessarily a global minimizer. However, with the condition that the object function of $F(u, f)$ in (3.6) is a linear combination of ℓ_1 and ℓ_2 norm terms with respect to u or f, a coordinatewise minimizer of $F(u, f)$ is also a global minimizer of $F(u, f)$. This result shown as Lemma 3.1 is a direct application of [83, Lemma 3.1] thus the proof of the result is omitted in this thesis.

Lemma 3.1. *Any coordinatewise minimizer of $F(u, f)$ defined by* (3.6) *is also a global minimizer.*

Since each subproblem of Algorithm 3 is not exactly solved, the function $F(u, f)$ is consequently not optimized. Therefore in the k-th iteration, given the error tolerance $\varepsilon_k > 0$ and $\delta_k > 0$ for optimizing u and f respectively, we have the following inequality:

$$\begin{aligned} F(u^{k+1}, f^k) &\le F(u^\star_{k+1}, f^k) + \varepsilon_k \\ F(u^{k+1}, f^{k+1}) &\le F(u^{k+1}, f^\star_{k+1}) + \delta_k, \end{aligned} \tag{3.7}$$

where $u^\star_{k+1} = \arg\min_u F(u, f^k)$ and $f^\star_{k+1} = \arg\min_f F(u^{k+1}, f)$. Then we can deduce a convergence theorem regarding to the sequence $\{(u^k, f^k)\}_k$ defined by (3.7).

Theorem 3.2. *Given $\sum_{j=0}^{\infty}(\varepsilon_j + \delta_j) < \infty$, the sequence $\{(u^k, f^k)\}_k$ defined by (3.7) is bounded and any of its cluster points is a global minimizer of $F(u, f)$.*

Proof. By (3.7), we have

$$\begin{aligned} F(u^{k+1}, f^{k+1}) &\le F(u^{k+1}, f^\star_{k+1}) + \delta_k \le F(u^{k+1}, f^k) + \delta_k \le F(u^\star_{k+1}, f^k) + \varepsilon_k + \delta_k \\ &\le F(u^k, f^k) + \varepsilon_k + \delta_k. \end{aligned}$$

Summing this inequality from 0 to k, we have

$$F(u^{k+1}, f^{k+1}) \le F(u^0, f^0) + \sum_{j=0}^{k}(\varepsilon_j + \delta_j).$$

By assumption, we have $\sum_{j=0}^{\infty}(\varepsilon_j + \delta_j) < \infty$. By the continuity and convexity of $F(u, f)$, it can be shown that all level sets of F, i.e. $\{(u, f) \in \mathcal{R}^n \times \mathcal{R}^m : F(u, f) \le C\}$, is compact. Therefore, the sequence $\{(u^k, f^k)\}_k$ is bounded and hence has a convergent subsequence. Without loss of generality, we assume that the sequence $\{(u^k, f^k)\}_k$ itself converges to a cluster point $(\bar{u}, \bar{f})$. Applying (3.7) again, we will have

$$\begin{aligned} F(u^{k+1}, f^k) &\le F(u^{k+1} + v_u, f^k) + \varepsilon_k \quad \forall v_u \in \mathcal{R}^n \\ F(u^{k+1}, f^{k+1}) &\le F(u^{k+1}, f^{k+1} + v_f) + \delta_k \quad \forall v_f \in \mathcal{R}^m. \end{aligned}$$

Let $k \to \infty$, $(u^k, f^k) \to (\bar{u}, \bar{f})$ and using the continuity of F bring out $F(u^k, f^k) \to F(\bar{u}, \bar{f})$. The assumption $\sum_{j=0}^{\infty}(\varepsilon_j + \delta_j) < \infty$ implies that $\varepsilon_k \to 0$ and $\delta_k \to 0$. Therefore, we have

$$\begin{aligned} F(\bar{u}, \bar{f}) &\le F(\bar{u} + v_u, \bar{f}) \quad \forall v_u \in \mathcal{R}^n \\ F(\bar{u}, \bar{f}) &\le F(\bar{u}, \bar{f} + v_f) \quad \forall v_f \in \mathcal{R}^m. \end{aligned}$$

As a result, the cluster point $(\bar{u}, \bar{f})$ is a coordinatewise minimizer of $F(u, f)$. Applying Lemma 3.1 we can prove that any cluster point $(\bar{u}, \bar{f})$ is also a global minimizer of $F(u, f)$. □

3.3 Numerical Results

This section is devoted to showing the superiority of the proposed isotropic wavelet frame based CT image reconstruction models to other alternating models. Subsection 3.3.1 will indicate the advantage of isotropic wavelet frame regularization to the anisotropic one. Moreover, Subsection 3.3.1 will also demonstrate the improvement of image quality by Radon domain inpainting mechanism. Subsection 3.3.2 will show that the proposed multi-system method (3.4) outperforms the popular FBP method and SART+TV method for the reconstruction of both the simulated phantom and the preclinical sheep lung. In particular, the proposed multi-system method has better preservation of sharp edges and more accurate approximation of smooth parts, which is consistent to the analysis of wavelet regularization to image restoration at the very beginning of Chapter 1. Subsection 3.3.3 will give the evidence showing that the multi-system method has good reconstruction quality for interior tomography problems.

3.3.1 CT Reconstruction by Radon Domain Inpainting Model

In this subsection, the proposed isotropic wavelet frame based CT image reconstruction models ((3.1) with $p = 2$ and (3.3) with $p = 2$) will be compared to the TV-based model (1.3) and the anisotropic wavelet frame based CT reconstruction model ((3.3) with $p = 1$). In particular, the model (3.1) with $p = 2$ includes the Radon domain inpainting mechanism while the model (3.3) does not. All the proposed and compared models are solved by the similar strategy of split Bregman algorithm. Therefore, the purpose of this subsection is to show that the advantage of isotropic wavelet frame regularization to the anisotropic wavelet frame and the TV regularization. Another goal of this subsection is to show the Radon domain inpainting can improve the quality of the reconstructed images.

In the experiments of this subsection, for the proposed model (3.1) with Radon domain inpainting , the parameters are set as $\kappa = 1, \lambda_2 = 0.01, \mu_2 = 0.00002, \mu_1 = 1000$. Only the parameter λ_1 is dependent on the strength of the noise and the number of projections. Stronger noise or less projection angles will correspond to relatively larger λ_1 as the optimal parameter settings. For the models (1.3) and (3.3) with both $p = 1$ and $p = 2$, the parameter λ is set the same as λ_1 in model

(3.1). These models are tested using a digital NURBS-based cardiac-torso (NCAT) phantom [73, 71, 72].

The projection data f for this subsection is generated by $f = P(\tilde{u}) + \epsilon$, where ϵ is some noise corresponding to an X-ray tube current of certain mA used in a typical scanning protocol [9]. Generally speaking, the noise at each pixel satisfies an Gaussian distribution with mean zero and a pixel-wise variance related to the intensity of the pixel. The following numerical simulations include the ϵ of two different noise levels: mild and strong noise levels (see Figure 3.1 for the noise distributions for 20 projections as an example). To help with easier observation of the noise level ϵ, we remark that the original intensity value of $P(\tilde{u})$ is in the range of $[0, 5.7613]$ with mean 2.3967.

In this subsections, the numerical comparison is based on the value of the relative error, the correlation and the total computational time. Given the reconstructed image u and the ground truth image $\tilde{u}$, the relative error and the correlation is defined as follows:

$$err(u) = \frac{\|u - \tilde{u}\|_2}{\|\tilde{u}\|_2} \tag{3.8}$$

$$corr(u) = \frac{(u - \bar{u})(\tilde{u} - \bar{\tilde{u}})}{\|u - u\|_2 \|\tilde{u} - \bar{\tilde{u}}\|_2} \tag{3.9}$$

where $\bar{u}$ and $\bar{\tilde{u}}$ denote the mean values of u and $\tilde{u}$ respectively.

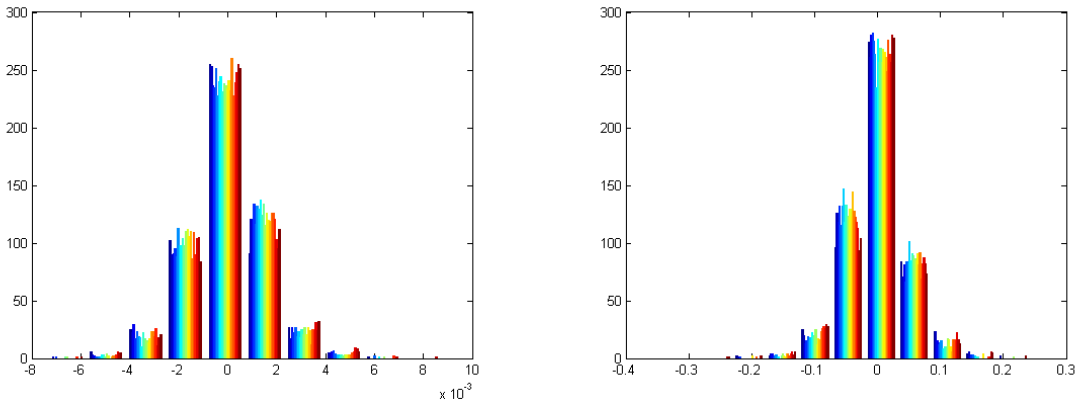

Figure 3.1: The distribution of the noise adding in the Radon domain with 20 projections. Images from left to right represent the mild and strong noise, respectively.

The reconstructed phantoms are shown in Figure 3.2 and 3.4, from which it can be seen that the reconstruction of both the isotropic wavelet frame based models ((3.1) with $p = 2$ and (3.3) with $p = 2$) has much less artifacts compared to TV

based model (1.3) and anisotropic wavelet frame based model ((3.3) with $p = 1$). Regarding to the reconstruction of the features, take $N_p = 15$ as an example, the TV based model loses almost all the features inside the lung but the other methods can recover some of the features. In particular, the isotropic wavelet frame based models can reconstruct more structure than the anisotropic one because the isotropic ℓ_1-norm can equally protect edges in all directions. Therefore, it has been demonstrated that the isotropic wavelet frame regularization is better than the TV and anisotropic wavelet frame regularization for CT image reconstruction problems.

Table 3.1 and 3.2 show the relative error and correlations for all the CT reconstruction models. It can be seen that the proposed Radon domain inpainting method (3.1) always has the lowest relative error and the highest correlation among all the models. Moreover, Figure 3.3 and 3.5 show the trend of the relative error during the execution of split Bregman iterations for all models, which gives us a conclusion that the Radon domain inpainting model (3.1) has the fastest decreasing speed of relative error with respect to the number of iterations. However, the computational time for Radon domain inpainting model (3.1) is nearly three times as other three models. Therefore, the Radon domain inpainting scheme is applicable for pursuing better quality of reconstruction with sufficient time limit. The isotropic wavelet frame based model ((3.3) with $p = 2$) without Radon domain inpainting is applicable for efficiently obtaining a good result although slightly worse than model (3.1). It should be claimed here that both the isotropic wavelet frame based model ((3.1) with $p = 2$ and (3.3) with $p = 2$) are proposed in [36] and this thesis as well.

Finally, using the model (3.1) to inpaint Radon domain twice can further reduce the relative error and improve the correlation while the time consumption will be even more than inpainting in Radon domain once (see Table 3.3).

Table 3.1: Comparison of relative error (in percentage), correlation (in percentage) and the running time (in seconds) of the algorithm with mild real noise.

N_p	TV-based Model			Anisotropic			Isotropic			Inpainting Model (3.1)		
	error	corr	Time	error	corr	Time	error	corr	Time	error	corr	Time
10	19.3	96.8	107	15.2	98.0	100	13.6	98.4	113	12.4	98.7	285
15	12.4	98.7	124	9.9	99.1	121	8.4	99.4	138	7.2	99.6	369
20	8.8	99.4	137	7.7	99.5	128	6.2	99.7	140	5.2	99.8	396
30	6.3	99.7	172	5.8	99.7	151	4.7	99.8	173	4.1	99.8	523
40	5.1	99.8	204	4.5	99.8	188	3.4	99.9	203	2.9	99.9	640
60	3.8	99.9	265	3.5	99.9	427	2.7	99.9	370	2.2	100.0	807

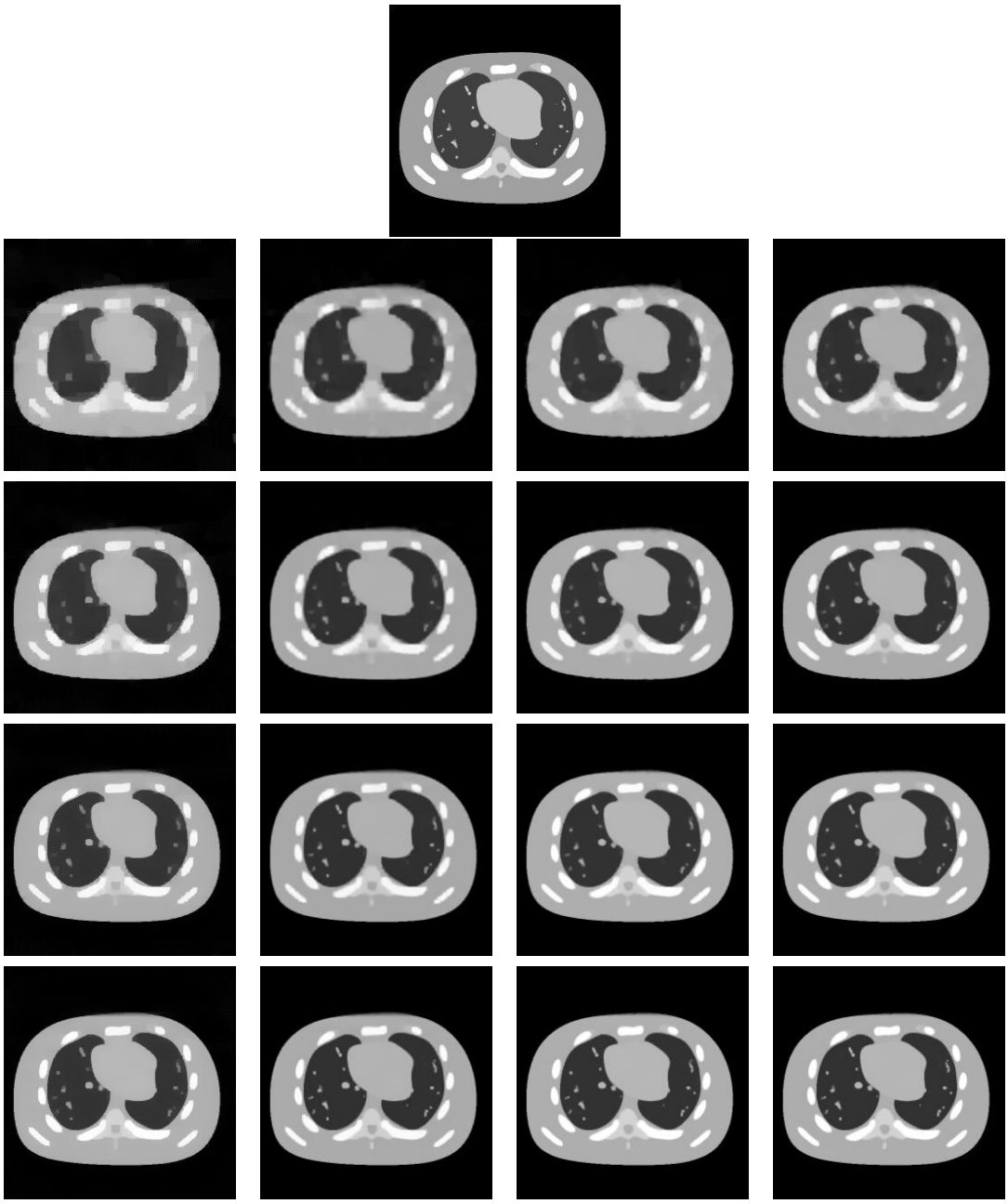

Figure 3.2: The tomographic result with mild real noise. The image on top is the true data $\tilde{u}$. The following rows represent the results using 15, 20, 30 and 40 projections, respectively. Images from left to right in each row are the results obtained by TV-based model, anisotropic wavelet frame based model, our proposed isotropic wavelet frame based model and our proposed model (3.1) with inpainting in Radon domain.

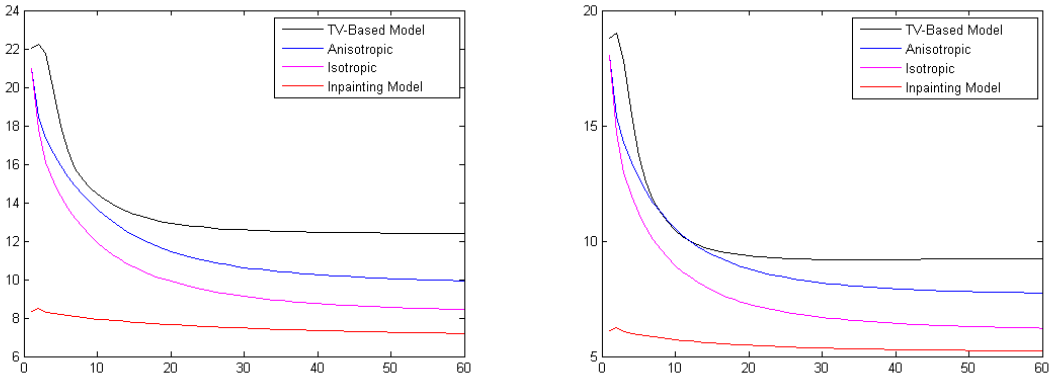

Figure 3.3: The change of relative error during the iteration for the cases with mild real noise. The two graphs represent the results using 15 and 20 projections, respectively.

Table 3.2: Comparison of relative error (in percentage), correlation (in percentage) and the running time (in seconds) of the algorithm with strong real noise.

N_p	TV-Based Model			Anisotropic			Isotropic			Inpainting Model (3.1)		
	error	corr	Time	error	corr	Time	error	corr	Time	error	corr	Time
15	15.3	98.1	146	11.1	99.0	130	10.2	99.1	126	9.5	99.2	338
20	12.6	98.6	295	8.9	99.3	142	8.2	99.4	159	7.9	99.4	430
30	11.2	98.9	354	7.5	99.5	186	7.1	99.6	177	7.0	99.6	526
40	10.4	99.1	398	7.1	99.6	218	6.6	99.6	207	6.5	99.6	654

Table 3.3: Comparison of relative error (in percentage), correlation (in percentage) and the running time (in seconds) of the multiple inpainting in Radon domain with the regularization of wavelet frame for mild real noise.

N_p	Isotropic			Inpainting Once			Inpainting Twice		
	error	correlation	Time	error	correlation	Time	error	correlation	Time
10	13.6	98.4	113	12.4	98.7	285	12.3	98.7	411
15	8.4	99.4	138	7.2	99.6	369	7.0	99.6	550
20	6.2	99.7	140	5.2	99.8	396	5.0	99.8	818

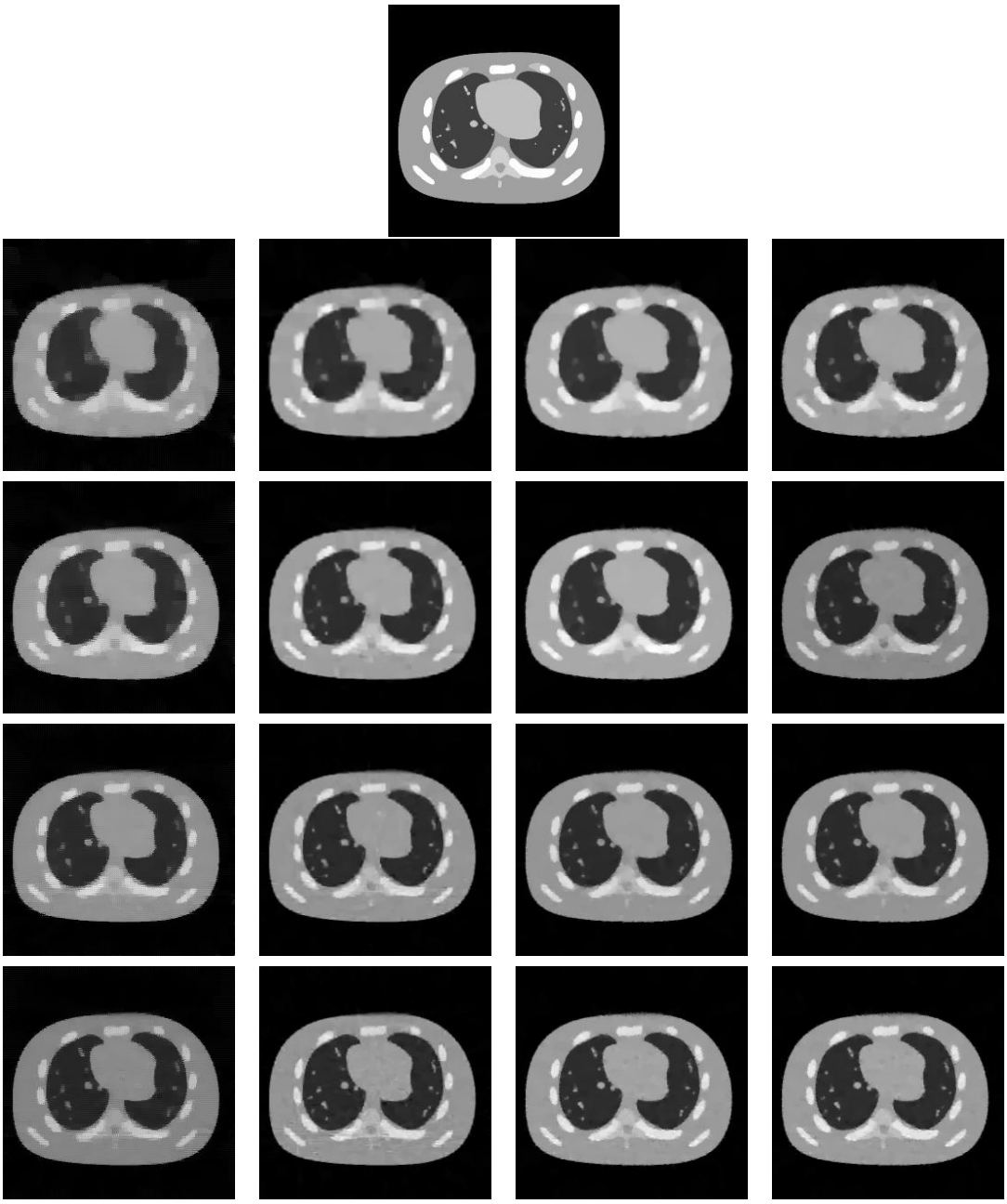

Figure 3.4: The tomographic result with strong real noise. The image on top is the true data $\tilde{u}$. The following rows represent the results using 15, 20, 30 and 40 projections, respectively. Images from left to right in each row are the results obtained by TV-based model, anisotropic wavelet frame based model and our proposed isotropic wavelet frame based model and our proposed model (3.1) with inpainting in Radon domain.

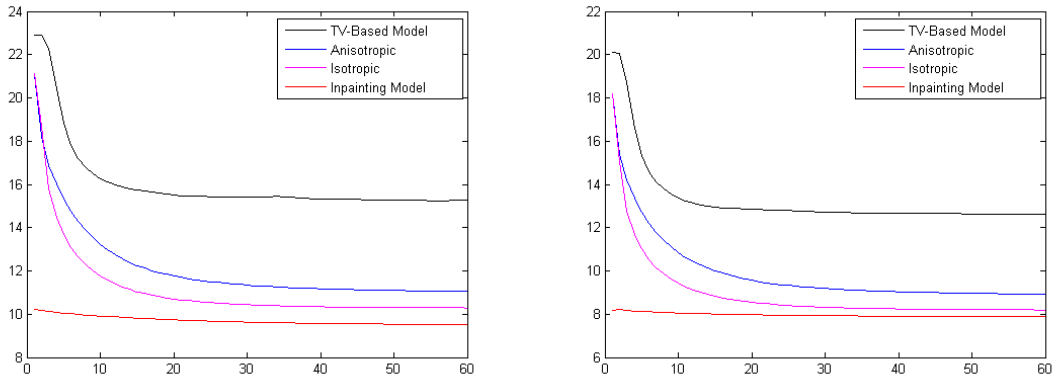

Figure 3.5: The change of relative error during the iteration for the cases with strong real noise. The two graphs represent the results using 15 and 20 projections, respectively.

3.3.2 CT Reconstruction by Multi-system Model

This subsection is devoted to the evaluation of the robust wavelet frame based model (3.4) by comparison to some popularly used methods such as the filtered back projection (FBP) and the simultaneous algebraic reconstruction technique method with total variation regularization (SART+TV). In this subsection, first a modified Shepp-Logan phantom which simulates a human head was chosen for the numerical simulations. The projection matrix P is generated from a typical SIEMENS fan-beam geometry including 672 detector cells and 1160 projections for a full scan. The measurements was polluted by Poisson noise which was simulated according to the physical imaging chain based method [88]. While the strength of Poisson noise is proportional to the number of photons, consequently the signal to noise ratio is inversely proportional to the photon number. The vector f was downsampled to using 75, 100, 150 and 200 projections from the original 1160 projections. After the numerical simulations of the simulated phantom, a preclinical projection f of a sheep lung scanned by a SIEMENS scanner [89] is also employed for the experiments.

In this subsection, similar as model (3.1), the parameters of (3.4) are also almost fixed for both the simulated phantom and the preclinical measurement. For example, the parameters for the artifacts and noise part is fixed as $\lambda_2 = 0.05, \lambda_3 = 10$ and the tolerance parameter ϵ is always 0.00001. The only exception is the parameter λ_1 which is dependent on the amount of features on the true image. In the numerical simulations of this subsection, $\lambda_1 = 4.0$ for the Shepp-Logan phantom and $\lambda_1 = 0.01$

for the preclinical sheep lung. The clear difference of the λ_1 for these two images is caused by that the preclinical sheep lung has more tiny features and less flat regions so that the optimal regularity should be relatively less than that for the Shepp-Logan phantom.

Besides the visual quality, the relative error (3.8) and the correlation (3.9), the mean structural similarity (SSIM) [90] and the CNR values are also applied to evaluate the quality of the CT image reconstructions. The structural similarity can be generally defined as in (3.10). In this thesis as well as most literatures, the mean SSIM is calculated by taking average of the SSIM values from different Gaussian windows with $hsize = 11$ and $\sigma = 1.5$.

$$SSIM(x, y) = \frac{(2\mu_x\mu_y + c_1)(2\sigma_x\sigma_y + c_2)}{(\mu_x^2 + \mu_y^2 + c_1)(\sigma_x^2 + \sigma_y^2 + c_2)} \tag{3.10}$$

where μ_x and μ_y are the average of the image patches x and y, respectively. σ_x and σ_y denote the variance of x and y. c_1 and c_2 are two constants to stabilize the division with weak denominator and their settings in this subsection are $c_1 = 0.01$ and $c_2 = 0.03$.

The CNR value is defined as the ratio between the intensity difference of two flat regions and the estimated noise standard deviation. Therefore, the CNR value is specially for evaluate the reconstruction of flat regions. The regions chosen for both the simulated Shepp-Logan phantom and the preclinical sheep lung are indicated by the circles in Figure 3.6. The ground truth of the Shepp-Logan phantom is selected as the phantom image. For the preclinical sheep lung study, reconstruction result by the FBP method from full 1160 projections is regarded as the ground truth.

To reconstruct an optimal result image of the preclinical sheep lung (with resolution 512×512), the canonical FBP method only needs 1.5 seconds from 100 projections. The SART+TV method takes 750 seconds for the same CT image reconstruction problem. Regarding to the proposed robust model (3.4), the total computational time is 422 seconds since only 10 iterations is sufficient to find a good object image.

Table 3.4 and 3.5 show the quantitative evaluation of the CT image reconstruction result. Compared to the FBP method and the SART+TV method, the proposed robust wavelet frame based model (3.4) always has the lowest relative error and the highest SSIM, correlation, and CNR value. The advantage of the proposed model (3.4) can be explained by that the isotropic wavelet frame regularization and the

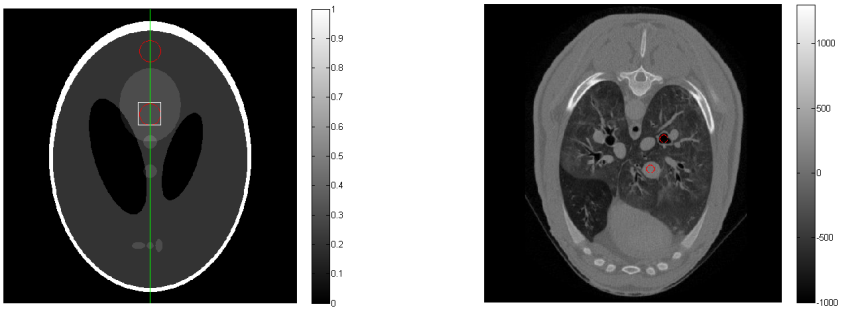

Figure 3.6: The ground truth images for numerical simulations. The left one is a modified Shepp-Logan phantom and the right one is a real sheep lung. The red circles indicate the regions for calculating the contrast-to-noise ratio (CNR). The white square indicates the magnified region of Figure 3.8. The green lines are the positions of the profiles in Figure 3.9.

three-system structure can remove most of the artifacts in different directions and protect most of the features such as the sharp edges. Moreover, Figure 3.7 and 3.11 visually show the advantage of the proposed model (3.4) which is consistent to the quantitative result shown in Table 3.4 and 3.5. In particular, Figure 3.8 and 3.9 show that in the flat region of ROI, the proposed method (3.4) has less error and standard deviation compared to the SART+TV method. Figure 3.10 also shows that the proposed analysis based method can preserve the sharp edge of the phantom while both the FBP method and the SART+TV oversmooth these edges. Furthermore, Figure 3.12 demonstrates that the separation of the three systems is appropriate. Figure 3.13 shows that the three-system method has less error than the single-system method ((3.3) with $p = 2$) without the terms of a and n.

Finally there is a remark that the Radon domain inpainting scheme can also improve the CT reconstruction results by removing more artifacts. However, such scheme will complicate the model (3.4) and computation time would be consequently increased to more than 4 times of the model (3.4) without Radon domain inpainting. Moreover, the effect of Radon domain inpainting is reduced if more noise is added to the initial measurement.

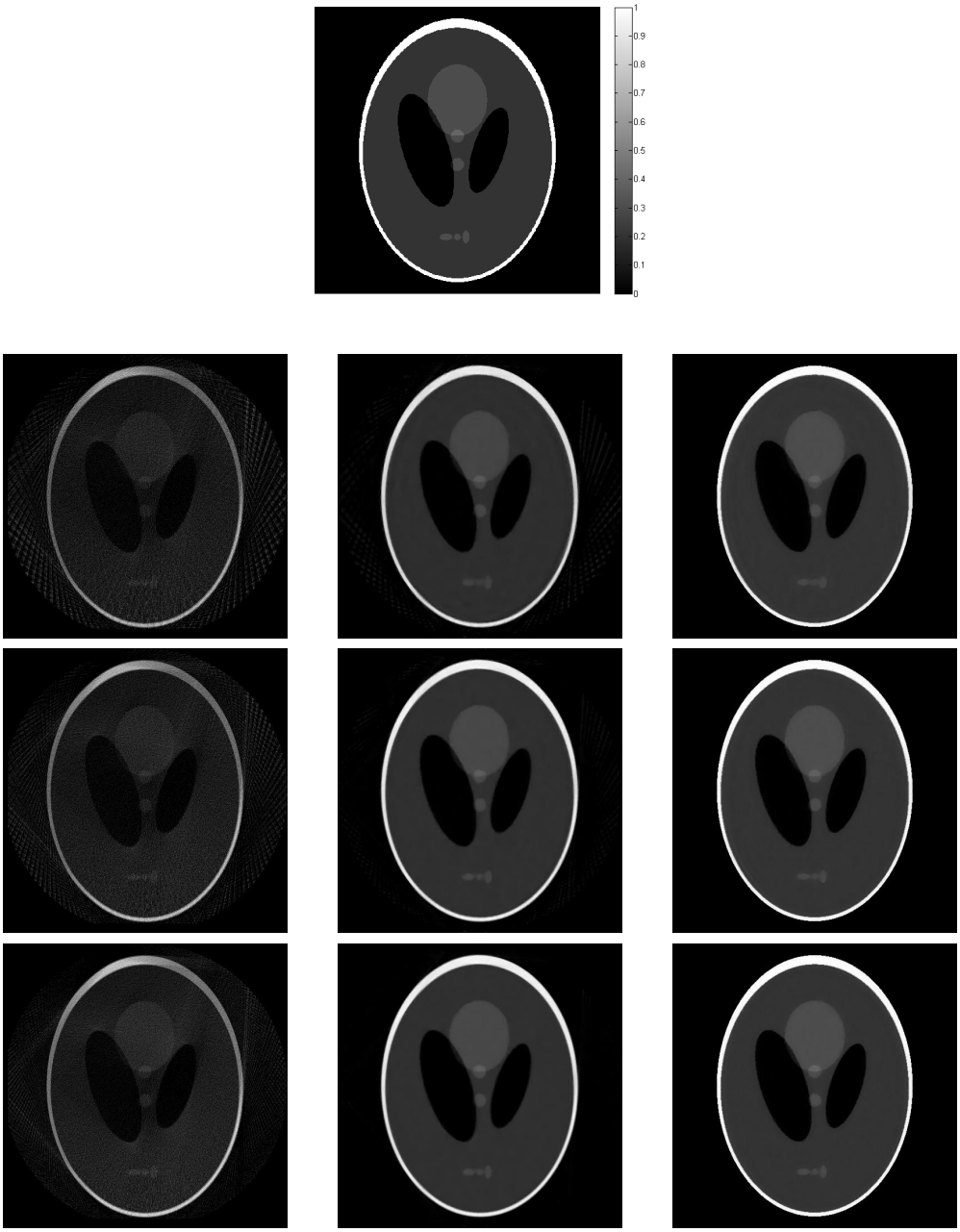

Figure 3.7: The tomographic results (512X512) of the Shepp-Logan phantom reconstructed from noisy projections with Poisson noise. The image on top is the ground truth image. The following rows are the CT reconstruction results using 75, 100 and 150 projections, respectively. Images from left to right in each row are the results obtained by FBP, SART with TV regularization and robust wavelet frame based model (3.4), respectively.

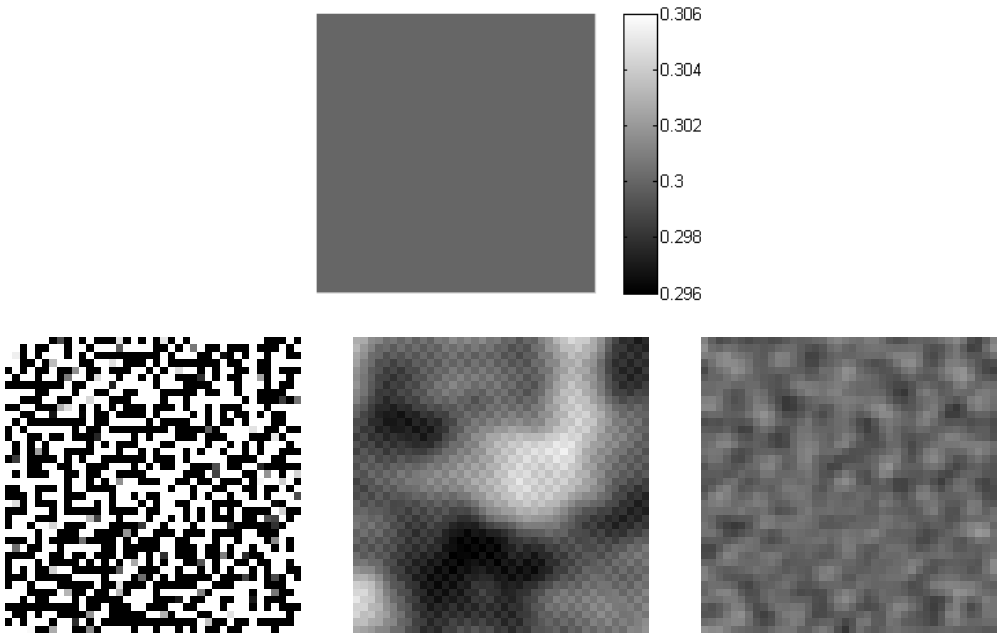

Figure 3.8: Zoom in images of a flat region of Figure 3.7 for 150 projections. The region is indicated in FIG 3.6. The image on top row is the ground truth image. For the bottom row, the images from left to right are the zoom in images obtained by FBP, SART with TV regularization and robust wavelet frame based model (3.4), respectively.

Table 3.4: Comparison of mean SSIM (Gaussian window of size 11 and standard deviation 1.5), relative error, correlation and contrast-noise-ratio (CNR) for the reconstructed results of the Shepp-Logan phantom from projections with Poisson noise.

N_p	FBP method				SART+TV method				Robust method (3.4)			
	SSIM	error	corr	CNR	SSIM	error	corr	CNR	SSIM	error	corr	CNR
75	0.623	0.582	0.865	509.4	0.946	0.246	0.969	1506.2	0.959	0.135	0.989	3015.4
100	0.637	0.548	0.883	569.8	0.949	0.228	0.969	1661.8	0.964	0.115	0.991	3389.0
150	0.658	0.500	0.899	651.4	0.950	0.227	0.969	1681.0	0.970	0.101	0.994	3938.1

Table 3.5: Comparison of mean SSIM (Gaussian window of size 11 and standard deviation 1.5), relative error, correlation and contrast-noise-ratio (CNR) for the reconstructed results of the preclinical sheep lung.

N_p	FBP method				SART+TV method				Robust method (3.4)			
	SSIM	error	corr	CNR	SSIM	error	corr	CNR	SSIM	error	corr	CNR
100	0.651	0.250	0.942	696.9	0.712	0.308	0.923	615.2	0.873	0.077	0.994	2332.3
150	0.709	0.262	0.954	787.4	0.727	0.264	0.932	639.9	0.899	0.061	0.996	2870.9
200	0.747	0.209	0.959	848.1	0.730	0.255	0.936	640.6	0.909	0.055	0.997	3136.9

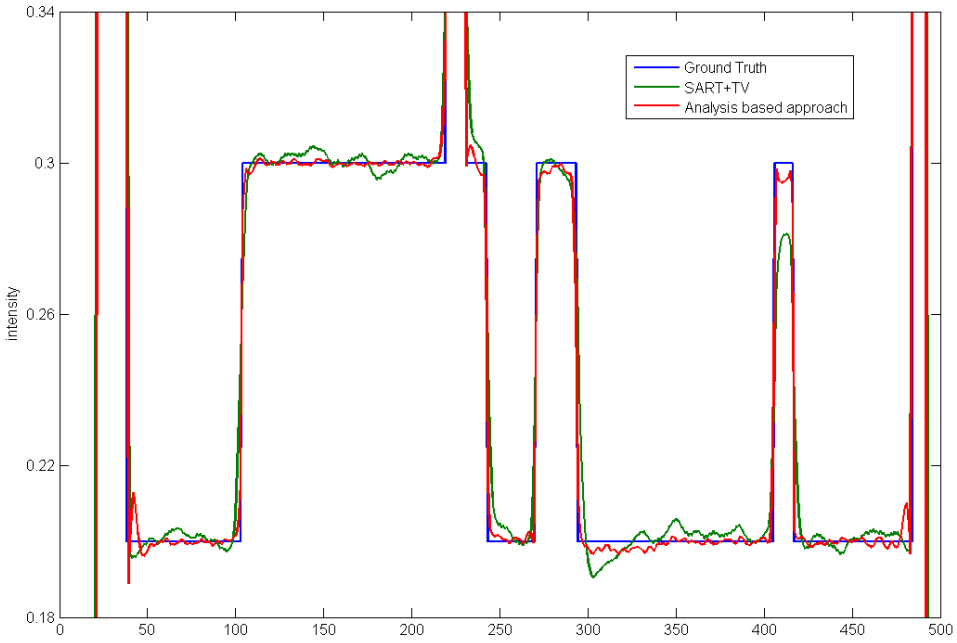

Figure 3.9: Representative of the profiles of the green line in the images in FIG 3.7 reconstructed from 150 projections.

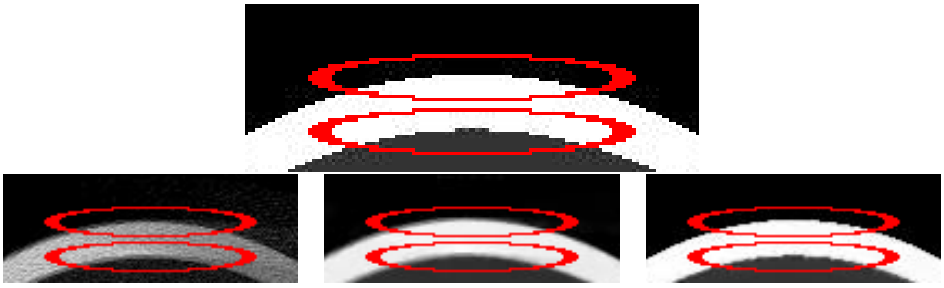

Figure 3.10: Zoom in images of the edge parts of Figure 3.7 for 150 projections. The image on top row is the zoom in part of assumed ground truth image. For the bottom row, images from left to right are the zoom in images obtained by FBP, SART with TV regularization and robust wavelet frame based model (3.4), respectively.

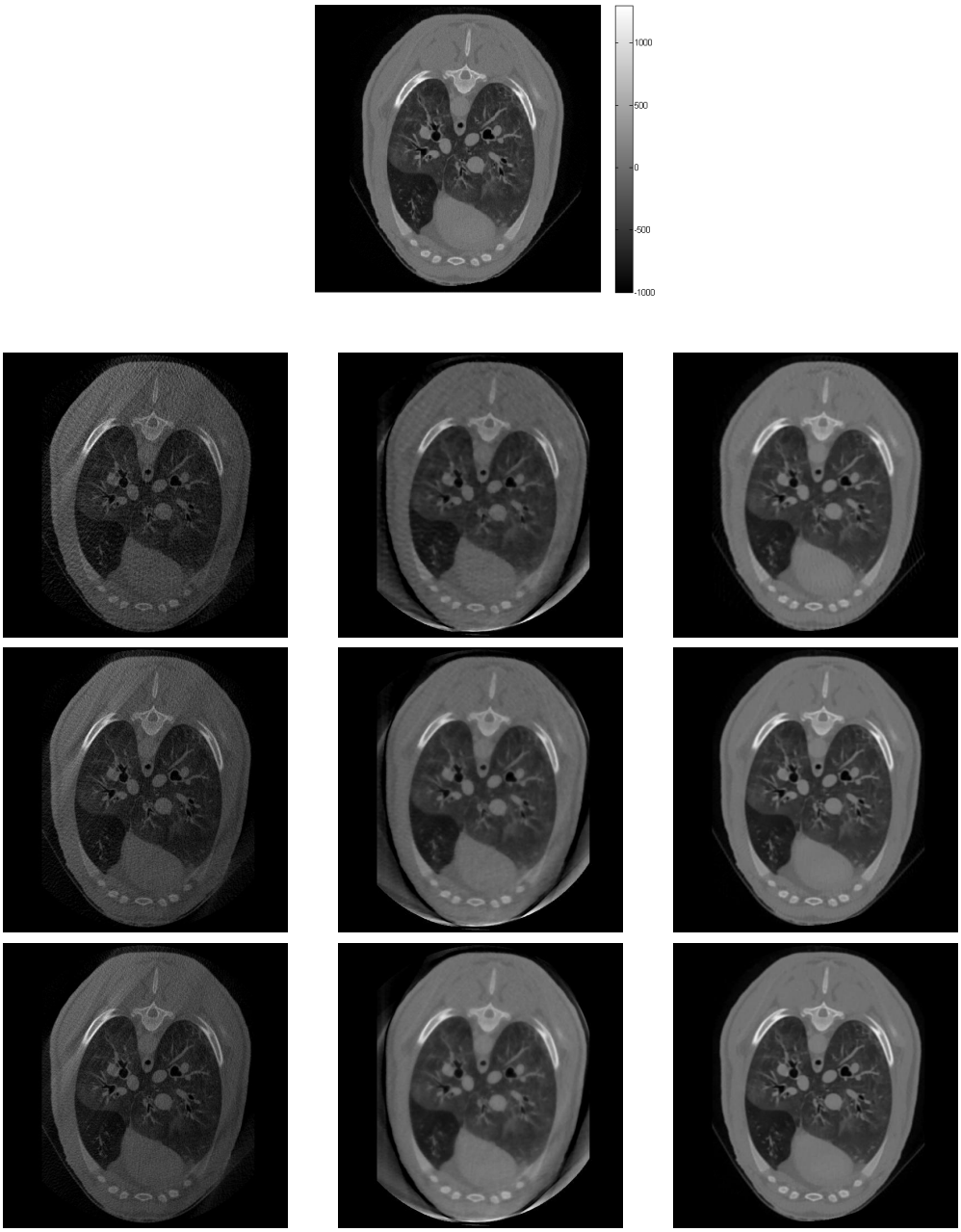

Figure 3.11: The tomographic results (512X512) of the real sheep lung. The image on top row is the ground truth image and the corresponding greymap bar (Hounsfield Unit). The following rows are the CT reconstruction results using 100, 150 and 200 projections, respectively. Images from left to right in each row are the results obtained by FBP, SART with TV regularization and robust wavelet frame based model (3.4), respectively.

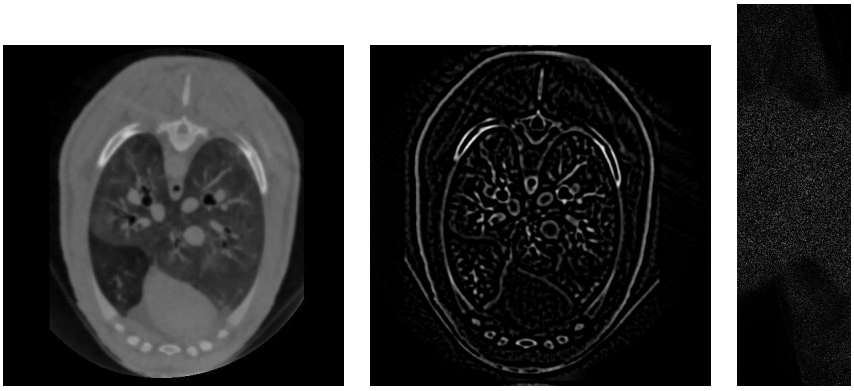

Figure 3.12: The separation of three parts of the image for real sheep lung reconstruction from 200 projections through the analysis based approach (3.4). The images from left to right are the image part, artifacts part and the noise part in the Radon domain.

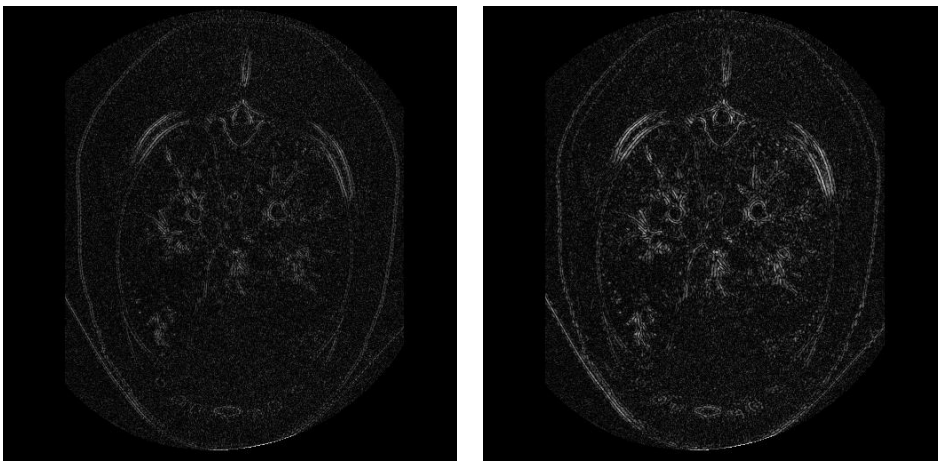

Figure 3.13: The error for the CT reconstruction of the sheep lung from 200 projections. The left image is the error of the proposed three-system method (3.4) and the relative difference is 0.055. The right image is the error and single-system method $\min_u \ \frac{1}{2}\|Pu - f\|_2^2 + \lambda_1 \|Wu\|_{1,2}$ and the relative difference becomes 0.069.

3.3.3 Interior Tomography Results

To simulate local projections for interior reconstruction, the middle 202 (30%) detector cells in each projection are extracted. Figure 3.14 and 3.15 show the interior tomography result for the Shepp-Logan phantom and the preclinical sheep lung, respectively. As well as the global reconstruction, it can be seen that the robust model (3.4) performs better than the FBP method and the SART+TV method. As a result, it can be claimed that the proposed robust wavelet frame based CT reconstruction model (3.4) is also applicable for the interior tomography problem.

3.4 Summary

In this chapter, two types of wavelet frame based CT reconstruction methods were proposed to reconstruct high quality CT reconstructed images with low projection dose. Fast and convergent algorithms for the proposed methods were also developed based on the split Bregman algorithm. Both numerical simulations and preclinical application were performed for the evaluation of different models and algorithms. It was shown in the numerical results that in terms of the visual quality, relative error and correlations, the proposed frame based methods can outperform anisotropic wavelet frame based method [58] and all TV regularized methods and un-regularized methods. The present study gives the possibility of reducing the CT projection dose while preserving the quality of the result images, which contributes to improving the precision of clinical diagnosis and reducing the X-ray exposure to the patients.

Regarding to the CT image reconstruction problem from highly insufficient number of projection angles, an isotropic wavelet frame based CT image reconstruction model (3.1) with Radon domain inpainting mechanism has been proposed in Subsection 3.1.1. Model (3.1) includes both the equation $Pu = f$ and the fidelity of Radon domain inpainting. Efficient algorithm which alternatingly optimizes the result image u and the inpainted Radon domain f was designed to solve the model (3.1). This thesis has also proved the convergence of the alternating optimization algorithm, i.e., the value of u and f can approach the their optimal solutions. Numerical simulations were executed using at least 10 projection angles of a digital NURBS-based cardiac-torso (NCAT) phantom [73, 71, 72]. Compared with the TV regularized method and anisotropic wavelet frame based method, the proposed method always

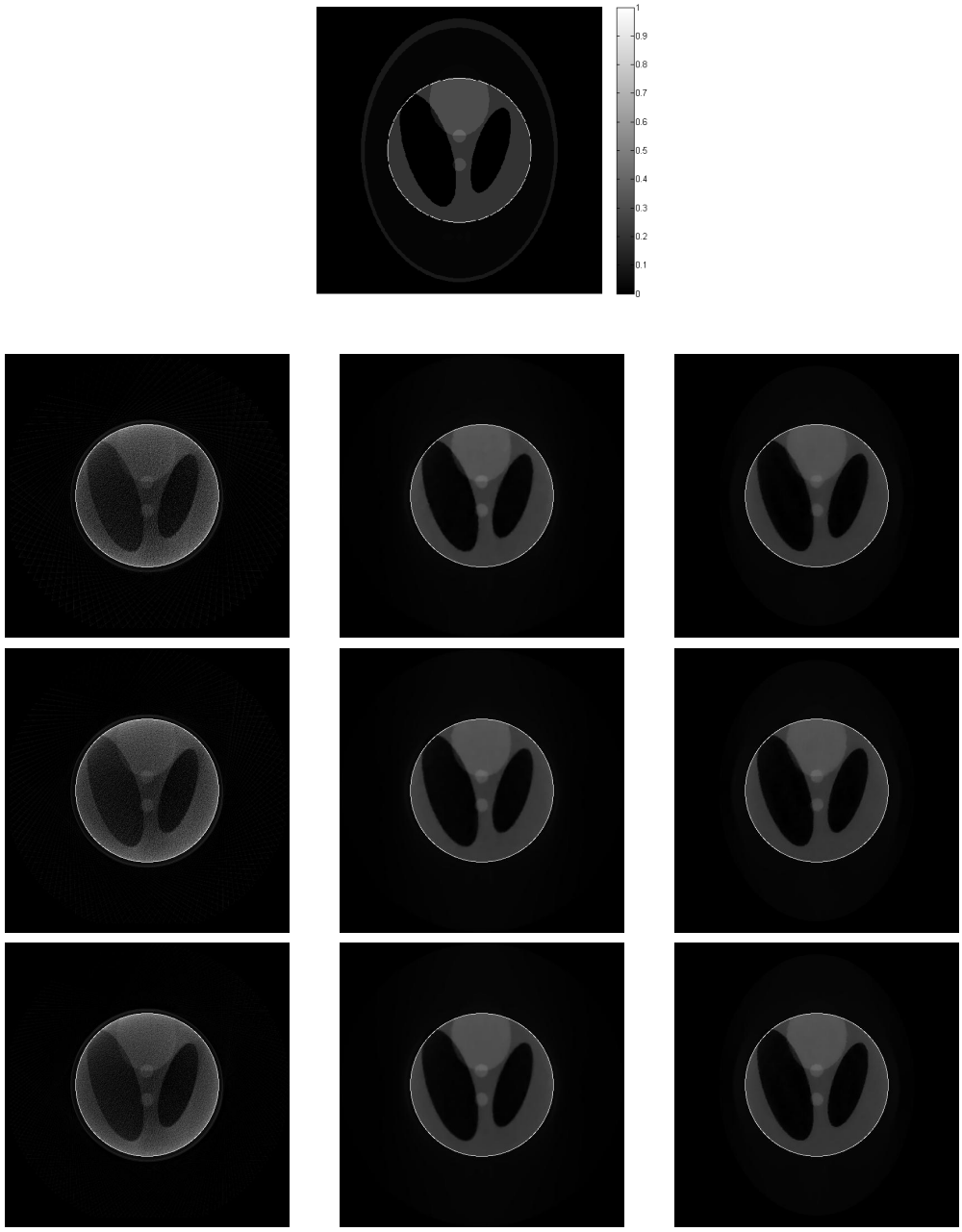

Figure 3.14: The interior tomographic results (512X512) of the Shepp-Logan phantom reconstructed from noisy projections with Poisson noise. The image on top row is the ground truth image. The following rows are the CT reconstruction results using 75, 100 and 150 projections, respectively. Images from left to right in each row are the results obtained by FBP, SART with TV regularization and robust wavelet frame based model (3.4), respectively. The highlighted parts in white circles centered at the middle of the phantom are the reconstructed ROI.

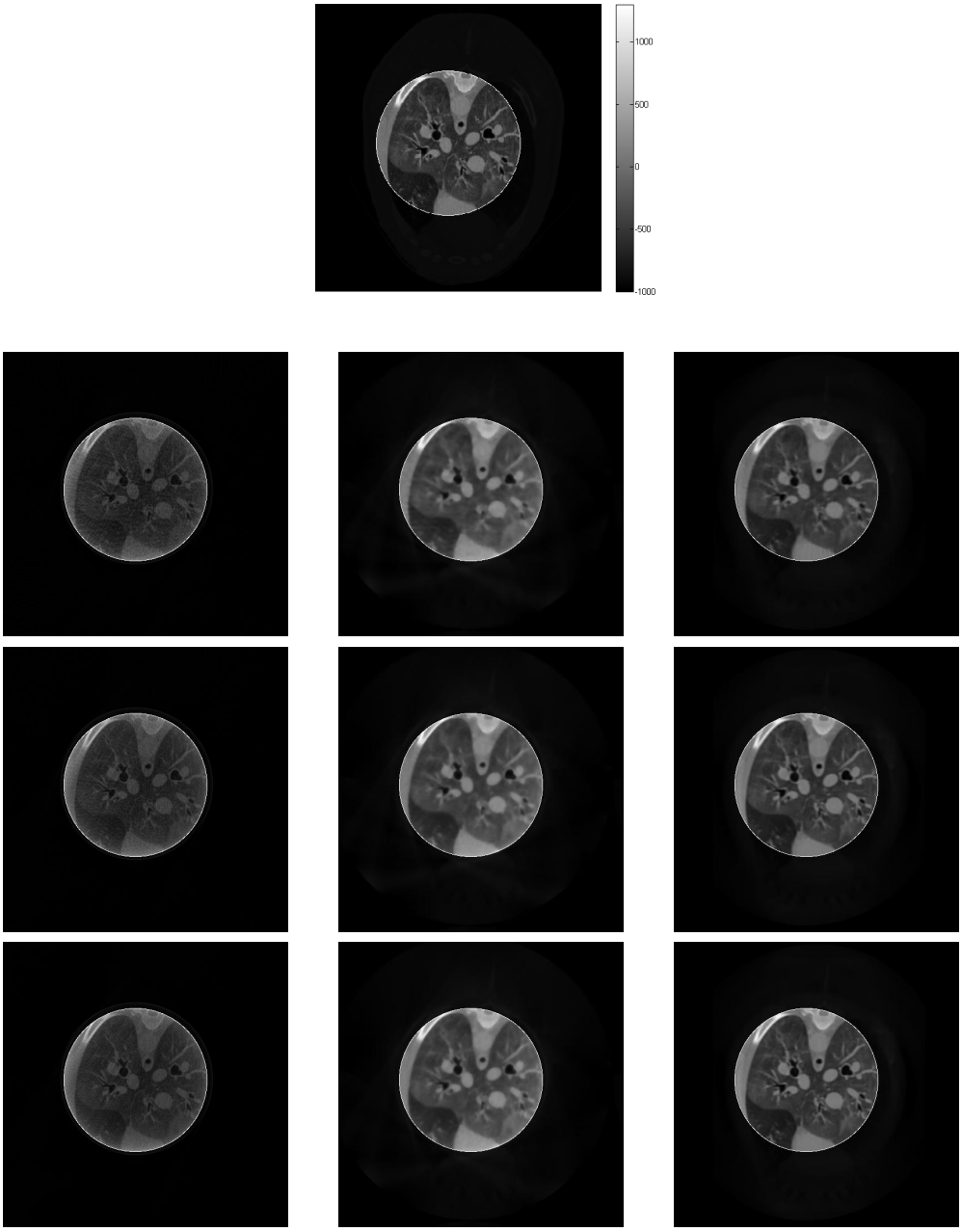

Figure 3.15: The interior tomographic results (512X512) of the real sheep lung. The image on top row is the ground truth image and the corresponding greymap bar (Hounsfield Unit). The following rows are the CT reconstruction results using 100, 150 and 200 projections, respectively. Images from left to right in each row are the results obtained by FBP, SART with TV regularization and robust wavelet frame based model (3.4), respectively. The highlighted parts in white circles centered at the middle of the phantom are the reconstructed ROI.

has lower relative error and higher correlations for the measurement with any small number of projections and any strength of additive noise in Subsection 3.2.1. Furthermore, the proposed method with Radon domain inpainting mechanism has the fastest decreasing speed of relative error. By applying Radon domain inpainting mechanism, it is possible to reduce approximately half of projection dose to preserve the same reconstruction quality compared with the TV regularized method. Compared with the most commonly used FBP method, the proposed method (3.1) can reduce even more proportion of projections while reconstructing images with even higher quality and less relative errors, which is significant for controlling the amount of radiation to the patients during cancer detection and radiation therapy. To be honest, the Radon domain inpainting mechanism inevitably complicates the model and algorithm, which would increase the time and memory consumption. The improved complexity of the model, however, could be accepted in the clinical application in merely several years thanks to the continuous development of hardware. Further research could investigate higher efficiency Radon domain inpainting algorithm to reduce the number of iterations and the time consumption.

Another problem highlighted in this chapter is the robustness to the inaccurate projection matrix P caused by the instrument error. To design an isotropic wavelet frame based robust CT reconstruction model, a three-system structure was introduced where the systems decompose the reconstructed images into three different parts: cartoon, artifacts and noise. When applying the three-system structure, the reconstructed images can be free from additive noise and artifacts caused by the inaccurate P. Besides the proposal of the robust isotropic wavelet frame based methods, this chapter also attempted to save more radiation dose by using the interior tomography scheme [85, 86] which illuminates a region-of-interest (ROI). By applying the corresponding efficient algorithms, this chapter accomplished some numerical simulations to the reconstruction of a real sheep lung which contains more complicated tiny features than the NCAT phantom. Numerical simulations showed that given the same amount of real measurement from a X-ray scanning machine, the proposed isotropic wavelet frame based methods were able to outperform two popular methods such as filtered back projection (FBP) method and the simultaneous algebraic reconstruction technique (SART) with total variation (TV) regularization (SART+TV) in terms of both the visibility and mean structural similarity. Moreover, the zoom-in figures show that the proposed isotropic wavelet frame based methods can preserve most of the useful tiny features when suppressing the noise

and artifacts. Compared with the NCAT phantom, the real sheep lung is closer to the current CT image reconstruction applications because of its complicated image structure and inaccurate measurement. Therefore, the good performance of the proposed isotropic wavelet frame based methods shown in Subsection 3.3.2 can improve the feasibility of applying wavelet frame based method to clinical applications. Furthermore, with the robustness of the proposed wavelet frame based CT image reconstruction model, it is possible to reduce the projection dose even if the projection matrix P has apparent instrument error caused by inaccurate beamlet location and direction. Additionally, Subsection 3.3.3 showed that our frame based models are applicable for interior tomography which can reduce more projection dose.

Chapter 4

Wavelets Approximation

The fundamental task of approximation is to approach a possibly complicated function called the target function by simpler functions. In particular, if the complicated function f satisfies some smooth condition, e.g., $f \in W_p^k(\mathcal{R}^s)$, then the quasi-projection operators generated by piece-wise polynomials can approximate f with certain approximation order. The quasi-projection operator has approximation order n if it can exactly reproduce polynomials of degree $n-1$ exactly. Section 4.1 will review the definition of quasi-projection operators and provide the conditions for exact reproduction of polynomials.

With the definition of B-spline refinable functions and its corresponding wavelets, the quasi-projection operator can be constructed by linear combination of B-spline refinable functions with the coefficients generated by wavelet decompositions [68, 37]. Section 4.2 will show that the quasi-projection operator with low frequency coefficients can approximate the smooth functions. Moreover, the quasi-projection operator with high frequency coefficients can approximate the derivatives of smooth functions. With the similar construction of 2-dimensional quasi-projection operators by tensor products, the approximation to 2-dimensional smooth functions and their partial derivatives can be similarly proved. The result of the approximation shows that the wavelet frame based image restoration models with the thresholding operation can generally preserve the information in the smooth image pieces. Since the sharp edges and features can be represented by large and sparse wavelet coefficients while the noises are represented by relatively smaller wavelet coefficients, the thresholding operation can also remove the additive noise while maintaining the

sharp edges. Therefore, the outperforming of wavelet frame based image restoration methods, including the numerical results shown in Chapter 2 and 3, can be theoretically explained.

In order to improve the approximation order of the quasi-projection operator without changing the inner product form $\langle f, \varphi_m^*(\cdot - \alpha)\rangle$ for P in (4.5) as well as the inner product form $\langle f, \psi_{m,l}(\cdot - \alpha)\rangle$ for Q_l in (4.8), it is necessary to design some new dual functions $\phi_{m,l,n}$ whose construction is similar as the pseudo-splines [33, 74]. Section 4.3 will give a general form and some examples of the dual function $\phi_{m,l,n}$ for pursuing higher approximation order n, where n can be arbitrarily high if the target function f is sufficiently smooth.

4.1 Approximation by Quasi-projection Operators

First, the quasi-projection operator Q without dilation is given by

$$Qf = \sum_{\alpha \in \mathbb{Z}^s} \langle f, \tilde{\phi}(\cdot - \alpha)\rangle \phi(\cdot - \alpha), \qquad f \in L_p(\mathcal{R}^s), \tag{4.1}$$

Then, the quasi-projection operator with dilation 2^j can be defined as

$$Q_j f = \sigma_{2^{-j}} Q \sigma_{2^j} f = 2^{js} \sum_{\alpha \in \mathbb{Z}^s} \langle f, \tilde{\phi}(2^j \cdot - \alpha)\rangle \phi(2^j \cdot - \alpha), \qquad f \in L_p(\mathcal{R}^s), \tag{4.2}$$

where the dilation operator can be defined as $\sigma_h f = f(\cdot/h)$ for all $h > 0$. First, we review the general theorem of approximation by quasi-projection operator proposed in [57] as follows:

Theorem 4.1. *([57] Theorem 3.1) Suppose $0 \le h < n$ and ϕ is a compactly supported function in $W_p^h(\mathcal{R}^s)$. Let Q and Q_j be the quasi-projection operator and its dilation defined as* (4.1) *and* (4.2)*, respectively. If $Qq = q$ for all $q \in \Pi_{n-1}$, then*

$$|f - Q_j f|_{h,p} \le C(2^{-j})^{n-h} |f|_{n,p} \qquad \forall f \in W_p^n(\mathcal{R}^s).$$

where $\|f\|_{n,p} = \sum_{h=1}^{n} |f|_{h,p}$ and $|f|_{h,p} = \sum_{|\mu|=h} \|D^\mu f\|_p$. In this chapter, $\|\cdot\|_{n,p}$ and $|\cdot|_{j,p}$ always represent the Sobolev norm and its corresponding semi-norms with $1 \le p \le \infty$. Π_{n-1} represents all the polynomials with order less than or equal to $n-1$. To obtain the condition $Qq = q$ for all $q \in \Pi_{n-1}$, we have the following

theorem whose condition is stated in Fourier domain.

Theorem 4.2. *([56, 37]) Let Q be the quasi-projection operator defined as* (4.1)*. Suppose that both of the following conditions hold:*

1. $\hat{\phi}(0) \neq 0$, and $D^{\mu}\hat{\phi}(2k\pi) = 0$, $\forall k \in \mathbb{Z}\backslash\{0\}$ and $|\mu| < n$, where D is the differential operator.

2. $D^{\mu}(1 - \hat{\tilde{\phi}}\overline{\hat{\phi}})(0) = 0 \quad \forall |\mu| < n$.

Then $Qq = q$ for all $q \in \Pi_{n-1}$.

The first condition (named Strang-Fix condition) can be equivalently stated as $[\hat{\phi}, \hat{\phi}] - |\hat{\phi}|^2 = O(|\cdot|)^{2n}$ with $[f, g](\xi) := \sum_{k\in\mathbb{Z}} f(\xi + 2\pi k)\overline{g(\xi + 2\pi k)}$. The second condition can also be equivalently stated as $1 - \hat{\tilde{\phi}}\overline{\hat{\phi}} = O(|\cdot|)^n$.

4.2 B-spline Wavelet Approximation

This section is devoted to proving the approximation of smooth functions and their derivatives by quasi-projection operators with B-spline refinable functions and wavelets. First we will introduce the definition of B-spline refinable functions and their corresponding wavelet functions. The Fourier transform of B-splines wavelet of order m and vanishing moment l are defined as:

$$\widehat{\psi_{m,l}}(\xi) := -i^l e^{-ij\frac{\xi}{2}} \sqrt{\binom{m}{l}} \frac{\cos^{m-l}(\xi/4)\sin^{m+l}(\xi/4)}{(\xi/4)^m} \tag{4.3}$$

where $j = m \bmod 2$. When $l = 0$, we denote the $\widehat{\psi_{m,0}}$ as the Fourier transform of the refinable function φ_m^* and

$$\widehat{\varphi_m^*}(\xi) = e^{-ij\frac{\xi}{2}} \frac{\sin^m(\xi/2)}{(\xi/2)^m} \tag{4.4}$$

it is clear that $\lim_{\xi\to 0} \widehat{\varphi_m^*}(\xi) = 1$ and $\varphi_m^* \in W_p^1(\mathcal{R})$ for $m \geq 2$. Moreover, regardless of the denominator, we can find that for B-spline function of order m, the Strang-Fix condition of order m must hold. Furthermore, consider the Taylor expansion of $\sin^m(\xi/2) = \frac{\xi}{2} - \frac{m}{6}(\frac{\xi}{2})^3 + O(\xi^5)$, we will know that for $\widehat{\varphi_m^*}$, the Taylor expansionwill have the form of $e^{-ij\frac{\xi}{2}}(a_0 + a_1(\frac{\xi}{2})^2 + O(\xi^2))$ where $a_0 = 1$ and a_1 is a non-zero real number. Moreover, the term $e^{-ij\frac{\xi}{2}}$ has absolute value 1. Therefore, we can only

have that $1 - |\widehat{\varphi_m^*}|^2 = O(|\cdot|)^2$. As a result, the B-spline functions of order $m \geq 2$ can generate the approximation order 2.

Now we give the definition of quasi-projection operator P and its dilated form P_j as follows:

$$Pf = \sum_{\alpha \in \mathbb{Z}} \langle f, \varphi_m^*(\cdot - \alpha) \rangle \varphi_m^*(\cdot - \alpha), \tag{4.5}$$

$$P_j f = 2^j \sum_{\alpha \in \mathbb{Z}} \langle f, \varphi_m^*(2^j \cdot - \alpha) \rangle \varphi_m^*(2^j \cdot - \alpha), \quad j \in \mathbb{Z}, \tag{4.6}$$

where φ_m^* is B-spline function of order $m \geq 2$ defined in (4.4). Then the m-th order Strang-Fix condition and $1 - |\widehat{\varphi_m^*}|^2 = O(|\cdot|)^2$ implies that $Pq = q$ for any linear polynomial q and P_j can approximate f with the approximation order 2. From the results above, we can state the theorem of approximation of smooth functions by quasi-projection operator of B-spline functions (see also [37]).

Theorem 4.3. *Suppose $f \in W_p^2(\mathcal{R})$ and $0 \leq h < 2$. Let P and P_j be the quasi-projection operator and its dilated form defined in* (4.5) *and* (4.6)*. Then*

$$|f - P_j f|_{h,p} \leq C(2^{-j})^{2-h} |f|_{2,p}. \tag{4.7}$$

In particular, $\|f - P_j f\|_p \leq C(2^{-j})^2 |f|_{2,p}$ for all $f \in W_p^2(\mathcal{R})$. Combining the cases of $h = 0$ and $h = 1$, we will have $\|f - P_j f\|_{1,p} \leq Ch|f|_{2,p} \leq Ch\|f\|_{2,p}$.

In the following part of this section, we focus on the approximation of derivatives by B-spine wavelet coefficients. To approximate the l-th order derivatives of functions, we define a quasi-projection operator Q_l and its dilated form $Q_{l,j}$ as follows:

$$Q_l f = a_l \sum_{\alpha \in \mathbb{Z}} \langle f, \psi_{m,l}(\cdot - \alpha) \rangle \varphi_m^*(\cdot - \alpha), \tag{4.8}$$

$$Q_{l,j} f = a_l 2^j \sum_{\alpha \in \mathbb{Z}} \langle f, \psi_{m,l}(2^j \cdot - \alpha) \rangle \varphi_m^*(2^j \cdot - \alpha), \tag{4.9}$$

where φ_m^* is B-spline function of order $m \geq 1$ defined in (4.4). $\psi_{m,l}$ is the corresponding B-spline wavelets with vanishing moment l defined in (4.3). a_l is a constant for the normalization of the quasi-projection operator. Then we want to prove that $Q_{l,j} = \sigma_{2^{-j}} Q_l \sigma_{2^j}$ can approximate the l-th order derivative of functions with approximation order of 2.

Consider the case of $l = 1$, notice that using integration by parts, we have

$$\langle f, \psi_{m,1}(\cdot - \alpha)\rangle = \int_{-\infty}^{\infty} f(x)\psi_{m,1}(x-\alpha)\mathrm{d}x = \int_{-\infty}^{\infty} f(x+\alpha)\mathrm{d}(\varphi_{m,1}(x))$$

$$= -\int_{-\infty}^{\infty} Df(x+\alpha)\varphi_{m,1}(x)\mathrm{d}x = -\int_{-\infty}^{\infty} Df(x)\varphi_{m,1}(x-\alpha)\mathrm{d}x = \langle Df, -\varphi_{m,1}(\cdot-\alpha)\rangle,$$

,where $D\varphi_{m,1} = \psi_{m,1}$. Therefore $\varphi_{m,1} = D^{-1}\psi_{m,1}$ which is a compactly supported function and in the Sobolev space $W_p^m(\mathcal{R})$ (since $\psi_1 \in W_p^{m-1}(\mathcal{R})$). Correspondingly, in Fourier domain, we have

$$\widehat{\varphi_{m,1}} = \widehat{\psi_{m,1}}/(i\xi) = -e^{-ij\frac{\xi}{2}}\frac{\sqrt{m}}{4}\frac{\cos^{m-1}(\xi/4)\sin^{m+1}(\xi/4)}{(\xi/4)^{m+1}} = -e^{-ij\frac{\xi}{2}}\frac{\sqrt{m}}{4}\frac{\sin^{m-1}(\xi/2)}{(\xi/2)^{m-1}}\frac{\sin^2(\xi/4)}{(\xi/4)^2}.$$

Since the Taylor expansions of both $\frac{\sin^{m-1}(\xi/2)}{(\xi/2)^{m-1}}$ and $\frac{\sin^2(\xi/4)}{(\xi/4)^2}$ have the form of $1+O(\xi^2)$, we have that

$$\widehat{\varphi_{m,1}}(\xi) = -e^{-ij\frac{\xi}{2}}\frac{\sqrt{m}}{4}(1+O(\xi^2)).$$

Together with the condition that $\overline{\widehat{\varphi_m^*}} = e^{ij\frac{\xi}{2}}\frac{\sin^m(\xi/2)}{(\xi/2)^m}$ we have $1 - (-\widehat{\frac{4}{\sqrt{m}}\varphi_{m,1}})\overline{\widehat{\varphi_m^*}} = O(\xi^2)$. Since φ_m^* also satisfies the Strang-Fix condition of order 2, by setting $a_1 = \frac{4}{\sqrt{m}}$, we have the result that

$$Q_1 f = \frac{4}{\sqrt{m}}\sum_{\alpha\in\mathbb{Z}}\langle f, \psi_{m,1}(\cdot-\alpha)\rangle\varphi_m^*(\cdot-\alpha) = \sum_{\alpha\in\mathbb{Z}}\langle Df, -\frac{4}{\sqrt{m}}\varphi_{m,1}(\cdot-\alpha)\rangle\varphi_m^*(\cdot-\alpha)$$

can exactly reproduce Df if $Df \in \Pi_1$ or $f \in \Pi_2$. For higher order derivatives, the calculation is similar and

$$Q_l f = \frac{4^l}{\sqrt{\begin{pmatrix} m \\ l \end{pmatrix}}}\sum_{\alpha\in\mathbb{Z}}\langle f, \psi_{m,l}(\cdot-\alpha)\rangle\varphi_m^*(\cdot-\alpha)$$

with $a_l = 4^l\binom{m}{l}^{-\frac{1}{2}}$ can exactly reproduce $D^l f$ if $D^l f \in \Pi_1$. As a result, the dilated quasi-projection operator $Q_{l,j}f$ defined in (4.9) can approximate $D^l f$ with

the approximation order never greater than 2, i.e.:

$$|Df - Q_{l,j}f|_{h,p} \leq C(2^{-j})^{n-h}|D^l f|_{n,p} \leq C(2^{-j})^{n-h}|f|_{n+l,p} \leq C(2^{-j})^{n-h}\|f\|_{k,p} \quad \forall f \in W_p^k(\mathcal{R}). \tag{4.10}$$

where $k \geq l$ and $n = \min(2, k-l)$. In particular, if $k = 2$ and $h = 0$, we have $\|Df - Q_{1,j}f\|_p \leq C2^{-j}|f|_{2,p}$ with approximation order 1. Here it should be noted that the idea of constructing the smooth fuction $\varphi_{m,1}$ by integrating $\psi_{m,1}$ was initially proposed in [77].

It is known that $\Psi_2 = \{\psi_{2,l}, 0 \leq l \leq 2\}$ with $m = 2$ form the linear B-spline wavelet system whose 2-dimensional form is frequently applied in Chapter 2 and 3 and other image restoration problems. By the results shown in (4.7) and (4.10), we can summarize the approximation of smooth functions and their derivatives as follows:

(i) if $f \in L_p(\mathcal{R})$, we can merely have the 0 order approximation of f as $\|f - P_j f\|_p \leq C\|f\|_p$.

(ii) if $f \in W_p^1(\mathcal{R})$, we can merely have the approximation of f as $\|f - P_j f\|_p \leq C2^{-r}|f|_{1,p}$ with approximation order 1. The approximation order of first order derivative is $|Df - Q_{1,j}f|_{h,p} \leq C|f|_{1,p}$ with approximation order 0.

(iii) if $f \in W_p^2(\mathcal{R})$, we can merely have the approximation of f as $\|f - P_j f\|_p \leq C(2^{-j})^2|f|_{2,p}$ with approximation order 2. The approximation order of the first order derivative is $|Df - Q_{1,j}f|_{h,p} \leq C2^{-j}|f|_{2,p}$ with approximation order 1. The approximation order of second order derivative is $|D^2 f - Q_{2,r}f|_{h,p} \leq C|f|_{2,p}$ with approximation order 0.

(iv) if $f \in W_p^k(\mathcal{R})$ with even larger k, the approximation order of f cannot exceed 2. The approximation of the derivatives can be correspondingly improved but also never greater than 2.

It can be easily observed that positive order of approximation implies the L_p convergence of the approximation. For example, $\|f - P_j f\|_p \leq C(2^{-j})^n|f|_{1,p}$ with $n > 0$ implies $\lim_{r\to\infty} P_j f = f$ in L_p sense. However, when $n = 0$, using the density of $C_0^\infty(\mathcal{R})$ in L_p space, we can prove that the equation $\lim_{r\to\infty} \|P_j f - f\| = 0$ also holds.

For the two-dimensional case which corresponds to the applications of image processing, by iteratively integrating the 2-dimensional wavelets ψ_{m,l_1,l_2}, the integrated

functions φ_{m,l_1,l_2} can be similarly calculated since the wavelets are defined by tensor product. The corresponding quasi-projector $Q_{l_1,l_2,j}f$ can also approximate the $\frac{\partial f}{\partial x_1{}^{l_1}\partial x_2{}^{l_2}}$ if f is sufficiently smooth. For the tight wavelet frame system, consider the normalization, it is known that the intensity value of the image is essentially regarded as $2^{j_0/2}\langle f, \tilde{\phi}(2^{j_0}\cdot - \alpha)\rangle$ for some position vector α and resolution level j_0. And one layer of 2-dimensional linear B-spline wavelet decomposition can be regarded as:

$$P_{j_0}f = P_{j_0-1}f + \sum_{0\le l_1,l_2\le 2, l_1l_2\neq 0}\sum_{\alpha\in\mathbb{Z}^2} 2^{2(j_0-1)}\langle f, \psi_{2,l_1,l_2}(2^{j_0-1}\cdot - \alpha)\rangle\psi_{2,l_1,l_2}(2^{j_0-1}\cdot - \alpha)$$

where $b_0(\alpha) = \langle f, \tilde{\varphi_2^*}(2^{j_0-1}\cdot - \alpha)\rangle, \alpha \in \mathbb{Z}^2$ represent the $2^{(-j_0+1)/2}$ multiple of the low frequency coefficients and $b_{l_1,l_2}(\alpha) = \langle f, \tilde{\psi_{2,l_1,l_2}}(2^{j_0-1}\cdot - \alpha)\rangle, \alpha \in \mathbb{Z}^2$ represent the $2^{(-j_0+1)/2}$ multiple of the wavelet coefficients or high frequency coefficients. Now it has been shown that in each smooth piece of images, when the low frequency coefficients b_0 in $P_{j_0-1}f$ approximates f, the high frequency coefficients b_l in $Q_{l_1,l_2,j_0-1}f$ simultaneously approximates the corresponding partial derivative. Such result shows that the wavelet decomposition can bring out good approximations of both functions and their derivatives in smooth image parts. Moreover, the wavelet coefficients $b_l(\alpha)$ can be regarded as good sample points of estimated derivative $D^l f$. In practice of image restorations, the wavelet frame based image restoration methods do not directly change the low frequency coefficients. Moreover, the high frequency coefficients are usually very close to 0 therefore the thresholding operation would not change these coefficients too much. Therefore, the smooth part of the image can be preserved from the fidelity information.

Regarding to the non-smooth part, or the edges and singularities in the images, although the above linear approximation theory is not applicable, the singularities of the underlying solutions can be represented by large wavelet coefficients while the remaining smooth pieces can be partitioned by these singularities. It is known that the sharp edges would correspond to large but sparse wavelet coefficients and the additive noise will bring a lot of small wavelet coefficients. Therefore, clear images with edges and without additive noises can be obtained through solving a solution only with a few large wavelet coefficients. In fact, in most popular wavelet frame regularized image restoration methods, including all the frame based methods in Chapter 2 and 3, there always exists one step called the shrinkage or thresholding operation (see equation (2.10) as an example) which is a non-linear approximation step to preserve the large wavelet coefficients, remove the small coefficients and

consequently approach a solution with sparse representation in wavelet transformed domain. Therefore, it is not surprising that the wavelet frame based image restoration method can preserve the smooth regions, sharp edges while suppressing the additive noise.

4.3 Higher Order Approximation

From Theorem 4.1 we know that given sufficiently smooth f, higher n for $Qq = q, q \in \Pi_{n-1}$ can correspond to higher approximation order. However, from equation (4.10), if we just choose ϕ as the B-spline refinable function φ_m^* as in previous sections, the approximation order of functions and their derivatives by P_j and $Q_{l,j}$ can be at most 2 due to not only the Strang-Fix condition but also the equation $1 - \widehat{\varphi_{m,l}}\overline{\widehat{\varphi_m^*}} = O(\xi^n)$ being not true for number $n > 2$. To obtain the approximation of $D^l f$ with higher approximation order up to n, we define the new dilated quasi-projection operator for functions and their derivatives as follows:

$$P_j^n f = 2^j \sum_{\alpha \in \mathbb{Z}} \langle f, \varphi_m^*(2^j \cdot - \alpha)\rangle \phi_{m,0,n}(2^j \cdot - \alpha)$$

$$Q_{l,j}^n f = a_l 2^j \sum_{\alpha \in \mathbb{Z}} \langle f, \psi_{m,l}(2^j \cdot - \alpha)\rangle \phi_{m,l,n}(2^j \cdot - \alpha) \tag{4.11}$$

where $m \geq 1$ and $1 \leq l \leq m$. Note that in (4.11), the inner product $\langle f, \psi_{m,l}(2^j \cdot - \alpha)\rangle$ represents the wavelet coefficients thus we should keep $\psi_{m,l}$ unchanged and find a better $\phi_{m,l,n}$ to satisfy both the Strang-Fix condition of order n and the equation $1 - \widehat{\varphi_{m,l}}\overline{\widehat{\phi_{m,l,n}}} = O(\xi^n)$. It can be observed that the approximated function $Q_{l,r}^n f$ is a piece-wise polynomial with degree n. In fact, if $f \in W_p^k(\mathcal{R})$, the approximation order of $D^l f$ by $Q_{l,j}^n$ can be improved to $n = k - l$ which is identical to the maximal approximation order of $D^l f$ by piece-wise polynomials with piece size 2^{-j} and degree $n = k - l$ (see the proof of Deny-Lions lemma in [1]).

4.3.1 Construction of Dual Functions

Here we first give the definition of $\widehat{\phi_{m,l,n}}$ as follows:

$$\widehat{\phi_{m,l,n}}(\xi) = e^{-ij\frac{\xi}{2}} \frac{\sin^k(\xi/2)}{(\xi/2)^k} \sum_{n=0}^{k-2} \alpha_n \sin^n(\xi/2) = e^{-i(j-j')\frac{\xi}{2}} \widehat{\varphi_n^*} \Theta(\sin(\xi/2)). \tag{4.12}$$

where φ_n^* is the B-spline function of order n and $\Theta(\sin(\xi/2)) = \Theta(\sin(\xi/2))_{m,l,n}$ is a trigonometric polynomial, $j = m \bmod 2$ and $j' = n \bmod 2$. Then in time domain, $\phi_{m,l,n}$ is the finite linear combination of integer translated n-th order B-spline function therefore $\phi_{m,l,n}$ lies in $W_p^{n-1}(\mathcal{R})$ and has compact support. Furthermore, $\phi_{m,l,n}$ satisfies the Strang-Fix condition of order n, i.e.:

$$[\widehat{\phi_{m,l,n}}, \widehat{\phi_{m,l,n}}] - |\widehat{\phi_{m,l,n}}|^2 = O(|\cdot|)^{2n}. \tag{4.13}$$

Notice that for $l \geq 0$ ($\varphi_{m,0} := \varphi_m^*$), $(\widehat{a_l\varphi_{m,l}})(\xi) = e^{-ij\frac{\xi}{2}} \frac{\sin^{m-l}(\xi/2)}{(\xi/2)^{m-l}} \frac{\sin^{2l}(\xi/4)}{(\xi/4)^{2l}}$, and $\sin^{2l}(\xi/4) = (\frac{1-\cos(\xi/2)}{2})^l = (\frac{\sin^2(\xi/2)}{2(1+\cos(\xi/2))})^l$. Therefore we have

$$((\widehat{-1)^l a_l\varphi_{m,l}})(\xi) = e^{-ij\frac{\xi}{2}} \frac{\sin^{m+l}(\xi/2)}{(\xi/2)^{m+l}} (\frac{2}{(1+\cos(\xi/2))})^l$$

and the corresponding $\widehat{\phi_{m,l,n}}(\xi)$ should approach

$$\frac{1}{\overline{((\widehat{-1)^l a_l\varphi_{m,l}})(\xi)}} = e^{-ij\frac{\xi}{2}} \frac{(\xi/2)^{m+l}}{\sin^{m+l}(\xi/2)} \frac{(1+\cos(\xi/2))^l}{2}.$$

Consequently, $\Theta(\sin(\xi/2))$ should approach

$$\frac{1}{e^{-i(j-j')\frac{\xi}{2}} \overline{((\widehat{-1)^l a_l\varphi_{m,l}})(\xi)} \widehat{\varphi_n^*}(\xi)} = \frac{e^{-ij\frac{\xi}{2}}}{e^{-i(j-j')\frac{\xi}{2}} e^{-ij'\frac{\xi}{2}}} \frac{(\xi/2)^{m+l+k}}{\sin^{m+l+k}(\xi/2)} \frac{(1+\cos(\xi/2))^l}{2}$$

$$= \frac{(\xi/2)^{m+l+k}}{\sin^{m+l+k}(\xi/2)} \frac{(1+\cos(\xi/2))^l}{2}.$$

Then we try to rewrite $\frac{1}{((\widehat{-1)^l a_l\varphi_{m,l}})(\xi)\widehat{\varphi_n^*}(\xi)}$ by the power series of $\sin(\xi/2)$ which is similarly occurred in [33].

Since $\arcsin\omega = \omega + \sum_{j=1}^{\infty} \frac{(2j-1)!!}{(2j)!!(2j+1)} \omega^{2j+1}$, we have

$$\xi/2 = \sin(\xi/2) + \sum_{j=1}^{\infty} \frac{(2j-1)!!}{(2j)!!(2j+1)} \sin^{2j+1}(\xi/2)$$

when $\xi \to 0$. Similarly, we can find the Maclaurin series of

$$1+\sqrt{1-\omega^2} = 2+\frac{1}{2}\omega^2+\sum_{j=2}^{\infty}\frac{(-1)^{j+1}(2j-3)!!}{(2j)!!}\omega^{2j}.$$

As a result, we have

$$1+\cos(\xi/2) = 2+\frac{1}{2}\sin^2(\xi/2)+\sum_{j=2}^{\infty}\frac{(-1)^{j+1}(2j-3)!!}{(2j)!!}\sin^{2j}(\xi/2)$$

when $\xi \to 0$. Summarize these results, we have:

$$\begin{aligned}\frac{1}{e^{-i(j-j')\frac{\xi}{2}}\overline{\widehat{((-1)^l a_l\varphi_{m,l})}(\xi)}\widehat{\varphi_n^*}(\xi)} = &\left[1+\sum_{j=1}^{\infty}\frac{(2j-1)!!}{(2j)!!(2j+1)}\sin^{2j}(\xi/2)\right]^{m+l+n}\\ &\left[1+\frac{1}{4}\sin^2(\xi/2)+\sum_{j=2}^{\infty}\frac{(-1)^{j+1}(2j-3)!!}{2(2j)!!}\sin^{2j}(\xi/2)\right]^{l}\end{aligned} \tag{4.14}$$

Therefore, we need to approach the Maclaurin series of $\frac{1}{e^{-i(j-j')\frac{\xi}{2}}\overline{\widehat{((-1)^l a_l\varphi_{m,l})}(\xi)}\widehat{\varphi_n^*}(\xi)}$ by its corresponding truncated polynomials. For a arbitrarily given positive even integer n, if we take $\Theta(\sin(\xi/2))$ to be the trigonometric polynomial of degree up to $n-2$, we will have the following result:

$$\Theta(\sin(\xi/2)) = \frac{1}{e^{-i(j-j')\frac{\xi}{2}}\overline{\widehat{((-1)^l a_l\varphi_{m,l})}(\xi)}\widehat{\varphi_n^*}(\xi)}+O(\sin(\xi/2)^n) = \frac{1}{e^{-i(j-j')\frac{\xi}{2}}\overline{\widehat{((-1)^l a_l\varphi_{m,l})}(\xi)}\widehat{\varphi_n^*}(\xi)}+O(\xi^n)$$

So we have

$$\widehat{((-1)^l a_l\varphi_{m,l})}(\xi)\overline{\widehat{\phi_{m,l,n}}(\xi)} = \widehat{((-1)^l a_l\varphi_{m,l})}(\xi)\left(\overline{e^{-i(j-j')\frac{\xi}{2}}\widehat{\varphi_n^*}(\xi)}\,\overline{\Theta(\sin(\xi/2))}\right) =$$

$$\overline{\left(e^{-i(j-j')\frac{\xi}{2}}\overline{\widehat{((-1)^l a_l\varphi_{m,l})}}\widehat{\varphi_n^*}\right)}\,\overline{\Theta(\sin(\xi/2))} = 1+O(\xi^n)$$

since $e^{-i(j-j')\frac{\xi}{2}}\overline{\widehat{((-1)^l a_l\varphi_{m,l})}}\widehat{\varphi_n^*} \to 1$ when $\xi \to 0$. Therefore, we already verified the approximation condition

$$1-\widehat{\varphi_{m,l}}(\xi)\overline{\widehat{\phi_{m,l,n}}(\xi)} = O(\xi^n). \tag{4.15}$$

Combining condition (4.13) and (4.15), we can generate the following theorem.

Theorem 4.4. *Suppose $f \in W_p^k(\mathcal{R})$ with $k \geq l$. Let $0 \leq n \leq k-l$ and define the quasi-projector $Q_{l,j}^n$ by (4.11), where the dual function $\phi_{m,l,n}$ is defined by (4.12). If $0 \leq h < n$, then*

$$|D^l f - Q_{l,j}^n f|_{h,p} \leq C(2^{-j})^{n-h}|D^l f|_{n+l,p} \leq C(2^{-j})^{n-h}|f|_{k,p} \leq C(2^{-j})^{n-h}\|f\|_{k,p}.$$

Note that the l and n can be arbitrarily large if k is large enough. In particular, take $h = 0$ and $n = k - l$, we have the L_p-norm approximation as the following corollary:

Corollary 4.5. *Suppose $f \in W_p^k(\mathcal{R})$ with $k \geq l$. Let $Q_{l,j}^{k-l}$ defined by (4.11). Then*

$$\|D^l f - Q_{l,j}^{k-l} f\|_p \leq C(2^{-j})^{k-l}|f|_{k,p} \leq C(2^{-j})^{k-l}\|f\|_{k,p}.$$

Summing up all the cases of $l = 0, 1, 2, \ldots, s \leq m$ in Corollary 4.5, the approximation of Sobolev norm $\|f\|_{s,p}$ can be described in the following corollary.

Corollary 4.6. *Given $f \in W_p^k(\mathcal{R})$ with $k \geq s + n$. Let $Q_{l,j}^n$ be defined as (4.11) for approximation of l-th order derivative. Then*

$$\left|\sum_{l=0}^{s} \|Q_{l,j}^n f\|_p - \|f\|_{s,p}\right| \leq \sum_{l=0}^{s} \left|\|Q_{l,j}^n f\|_p - \|D^l f\|_p\right|$$
$$\leq \sum_{l=0}^{s} C(2^{-j})^n |f|_{2+l,p} \leq C(2^{-j})^n \|f\|_{2+s,p} \leq C(2^{-j})^n \|f\|_{k,p}.$$

4.3.2 Some Examples

Regarding to the form of $\widehat{\phi_{m,l,n}}$ shown in (4.12), it is necessary to generate the trigonometric polynomial $\Theta(\sin(\xi/2))$ by truncating the series shown in (4.14). Take $m = 2, l = 1, n = 4$ as an example, $\psi_{2,1}$ is the linear B-spline wavelets with vanishing moment 1. Section 4.3 already shows that

$$Q_{1,j} f = Q_{1,j}^2 f = \frac{4}{\sqrt{2}} 2^j \sum_{\alpha \in \mathbb{Z}} \langle f, \psi_{2,1}(2^j \cdot - \alpha)\rangle \varphi_2(2^j \cdot - \alpha)$$

can approximate Df with approximation order 2 for $f \in W_p^3(\mathcal{R})$. If the function f has better smoothness condition, e.g., $f \in W_p^5(\mathcal{R})$, it is possible to enhance the approximation order from 2 to 4. However, the improvement of approximation order also needs to replace the last term $\varphi_2(2^j \cdot - \alpha)$ by $\phi_{2,1,4}(2^j \cdot - \alpha)$. By checking the

equation (4.14) and truncate the trigonometric polynomial $\sin^{2j}(\xi/2)$ with power up to $4-2=2$, we have the following statement:

$$\frac{1}{\widehat{((-\frac{4}{\sqrt{2}})^1\varphi_{2,1})}(\xi)\widehat{\varphi_4^*}(\xi)} = \left[1+\tfrac{1}{6}\sin^2(\xi/2)+O(\xi^4)\right]^7$$
$$\left[1+\tfrac{1}{4}\sin^2(\xi/2)+O(\xi^4)\right]^1 = 1+\tfrac{17}{12}\sin^2(\xi/2)+O(\xi^4).$$

Note that $e^{i(j-j')\frac{\xi}{2}}=1$ since $j=m \mod 2=0$ and $j'=n \mod 2=0$. Therefore, $\Theta(\sin(\xi/2))=1+\frac{17}{12}\sin^2(\xi/2)$ and the Fourier transform of the function $\phi_{2,1,4}$ can be consequently defined as

$$\widehat{\phi_{2,1,4}}(\xi)=\widehat{\varphi_4^*}(\xi)(1+\frac{17}{12}\sin^2(\xi/2)) \tag{4.16}$$

where φ_4^* is the cubic B-spline function. Observe that $\sin^2(\xi/2)=\left[\frac{e^{i\xi/2}-e^{-i\xi/2}}{2i}\right]^2 = \frac{e^{i\xi}-2+e^{-i\xi}}{-4}=\frac{1}{2}-\frac{e^{i\xi}+e^{-i\xi}}{4}$. Moreover, the inverse Fourier transforms of complex functions $e^{\pm i\xi}$ are nothing but translation by distance ∓ 1, or shift by one unit to both directions. In another word, the equation (4.16) can be equivalently described in the time domain as follows:

$$\phi_{2,1,4}(x)=\frac{41}{24}\varphi_4^*(x)-\frac{17}{48}(\varphi_4^*(x-1)+\varphi_4^*(x+1)),$$

It can be seen that $\phi_{2,1,4}(x)$ is also a compactly supported piece-wise cubic polynomial. Moreover, the discontinuous points are all integer points, which is important for the linear approximation theory and its application to discretized image processing problems. As a result, the quasi-projection operator

$$Q_{1,j}^4 f = 2\sqrt{2}\cdot 2^j\sum_{\alpha\in\mathbb{Z}}\langle f,\psi_{2,1}(2^j\cdot-\alpha)\rangle\phi_{2,1,4}(2^j\cdot-\alpha)$$

has the property

$$|Df-Q_{1,j}^4 f|_p \le C(2^{-j})^4|Df|_{4,p}\le C(2^{-j})^4\|f\|_{5,p}, \forall f\in W_p^5(\mathcal{R}).$$

For the second example, we set $m=1, l=1$ and $n=4$, which is to show that given enough smoothness condition, the approximation order can be arbitrarily high

for even the Haar wavelet. For this case, we can generate the following equations:

$$\frac{1}{e^{-i(j-j')\frac{\xi}{2}}\overline{((-\widehat{\frac{4}{\sqrt{1}})^1\varphi_{1,1}})(\xi)\widehat{\varphi_4^*}}}(\xi) = \left[1+\tfrac{1}{6}\sin^2(\xi/2)+O(\xi^4)\right]^6$$
$$\left[1+\tfrac{1}{4}\sin^2(\xi/2)+O(\xi^4)\right]^1 = 1+\tfrac{5}{4}\sin^2(\xi/2)+O(\xi^4)$$

Since m is odd and n is even, we have $e^{-i(j-j')\frac{\xi}{2}}=e^{-i\frac{\xi}{2}}$ and

$$\widehat{\phi_{1,1,4}}(\xi) = e^{-i\frac{\xi}{2}}\widehat{\varphi_4^*}(\xi)(1+\frac{5}{4}\sin^2(\xi/2)) \tag{4.17}$$

In time domain, equation (4.17) can be rewritten as:

$$\phi_{1,1,4}(x) = \frac{13}{8}\varphi_4^*(x-\frac{1}{2}) - \frac{5}{16}(\varphi_4^*(x-\frac{3}{2})+\varphi_4^*(x+\frac{1}{2}))$$

where φ_4^* is the cubic B-spline function. The half shift existed at all the terms since the Haar wavelet itself contains half shift. Based on this definition, the quasi-projection operator

$$Q_{1,j}^{4*}f = 4\cdot 2^j\sum_{\alpha\in\mathbb{Z}}\langle f,\psi_{1,1}(2^j\cdot-\alpha)\rangle\phi_{1,1,4}(2^j\cdot-\alpha)$$

also satisfies

$$|Df-Q_{1,j}^{4*}f|_p \le C(2^{-j})^4|Df|_{4,p} \le C(2^{-j})^4\|f\|_{5,p}, \forall f\in W_p^5(\mathcal{R})$$

although the Haar wavelets $\psi_{1,1}$ has worse properties than linear B-spline wavelet $\psi_{2,1}$.

A final remark of this subsection is that the formula of $\phi_{4,0,4}(0)$ can be similarly calculated and the result $\Theta(\sin(\xi/2)) = 1+\frac{4}{3}\sin^2(\xi/2)$ is consistent to that in [33].

4.4 Summary

This chapter is devoted to the approximation of derivatives and Sobolev norms of smooth functions via quasi-projection operators constructed from B-spline wavelets. First, using the method from [77] we integrated the B-spline wavelet $\psi_{m,l}$ by l times to generate a smooth function $\varphi_{m,l}$ with vanishing moment 0. Then we showed that both the Strang-Fix condition $[\widehat{\phi_{m,l,n}},\widehat{\phi_{m,l,n}}]-|\widehat{\phi_{m,l,n}}|^2 = O(|\cdot|)^{2n}$ and the

approximation condition $1 - \widehat{\varphi_{m,l}}\overline{\widehat{\phi_{m,l,n}}} = O(|\cdot|)^n$ hold for appropriately constructed $\phi_{m,l,n}$. In particular, $k = \max(2, m)$ if the $\phi_{m,l,n}$ is simply chosen as the B-spline refinable functions φ_m. Moreover, Section 4.3 provided a general formula of $\phi_{m,l,n}$ for pursuing arbitrarily high approximation order n. Given a wavelet $\psi_{m,l}$ and n, the constructed function $\phi_{m,l,n}$, generated by finite linear combination of integer shifted n-th order B-spline functions, is a n-th order piece-wise polynomial with compact support. The approximation result can be further applied to the discrete case such as in signal and image processing. Higher approximation order can obtain better approximation to the singularities or features so that the wavelet decomposition layers can be reduced to deduct time and memory consumption.

Bibliography

[1] R. A. Adams and J. J. Fournier, *Sobolev spaces*, vol. 140, Access Online via Elsevier, 2003.

[2] S. Alliney, *Digital filters as absolute norm regularizers*, IEEE Transactions on Signal Processing, 40 (1992), pp. 1548–1562.

[3] L. Bar, N. Kiryati, and N. Sochen, *Image deblurring in the presence of impulse noise*, International Journal of Computer Vision, 70 (2006), pp. 279–298.

[4] L. Bar, N. Sochen, and N. Kiryati, *Image deblurring in the presence of salt-and-pepper noise*, in Lecture Notes in Computer Science, Scale Space and PDE Methods in Computer Vision, LNCS), vol. 3459, 2005, pp. 107–118.

[5] M. Bertalmio, A. L. Bertozzi, and G. Sapiro, *Navier-stokes, fluid dynamics, and image and video inpainting*, in Computer Vision and Pattern Recognition, 2001. CVPR 2001. Proceedings of the 2001 IEEE Computer Society Conference on, vol. 1, IEEE, 2001, pp. I–355.

[6] M. Bertalmio, G. Sapiro, V. Caselles, and C. Ballester, *Image inpainting*, (2000), pp. 417–424.

[7] M. Bertalmio, L. Vese, G. Sapiro, and S. Osher, *Simultaneous structure and texture image inpainting*, IEEE Transactions on Image Processing, 12 (2003), pp. 882–889.

[8] J. Bezdek and R. Hathaway, *Convergence of alternating optimization*, Neural, Parallel & Scientific Computations, 11 (2003), pp. 351–368.

[9] J. T. Bushberg, J. A. Seibert, E. M. Leidholdt Jr, J. M. Boone, and E. J. Goldschmidt Jr, *The essential physics of medical imaging*, Medical Physics, 30 (2003), p. 1936.

[10] J. Cai, R. Chan, L. Shen, and Z. Shen, *Convergence analysis of tight framelet approach for missing data recovery*, Advances in Computational Mathematics, (2008), pp. 1–27.

[11] J. Cai, R. Chan, and Z. Shen, *A framelet-based image inpainting algorithm*, Applied and Computational Harmonic Analysis, 24 (2008), pp. 131–149.

[12] J. Cai, R. H. Chan, and Z. Shen, *Simultaneous cartoon and texture inpainting*, Inverse Probl. Imaging, 4 (2010), pp. 379–395.

[13] J. Cai, B. Dong, S. Osher, and Z. Shen, *Image restorations: total variation, wavelet frames and beyond*, Journal of the American Mathematical Society, 25(4) (2012), pp. 1033–1089.

[14] J. Cai, M. Nikolova, and R. Chan, *Fast two-phase image deblurring under impulse noise*, J. Math. Imaging Vis., 36 (2010), pp. 46–53.

[15] J. Cai, S. Osher, and Z. Shen, *Linearized Bregman iterations for compressed sensing*, Math. Comp, 78 (2009), pp. 1515–1536.

[16] ——, *Split Bregman methods and frame based image restoration*, Multiscale Modeling and Simulation: A SIAM Interdisciplinary Journal, 8 (2009), pp. 337–369.

[17] E. Candes and D. Donoho, *New tight frames of curvelets and optimal representations of objects with C2 singularities*, Comm. Pure Appl. Math, 56 (2004), pp. 219–266.

[18] A. Chai and Z. Shen, *Deconvolution: A wavelet frame approach*, Numerische Mathematik, 106 (2007), pp. 529–587.

[19] A. Chambolle, *An algorithm for total variation minimization and applications*, Journal of Mathematical Imaging and Vision, 20 (2004), pp. 89–97.

[20] R. Chan, T. Chan, L. Shen, and Z. Shen, *Wavelet algorithms for high-resolution image reconstruction*, SIAM Journal on Scientific Computing, 24 (2003), pp. 1408–1432.

[21] R. Chan, S. Riemenschneider, L. Shen, and Z. Shen, *Tight frame: an efficient way for high-resolution image reconstruction*, Applied and Computational Harmonic Analysis, 17 (2004), pp. 91–115.

[22] R. Chan, L. Shen, and Z. Shen, *A framelet-based approach for image inpainting*, Research Report, 4 (2005), p. 325.

[23] T. Chan and S. Esedoglu, *Aspects of Total Variation Regularized L'Function Approximation*, SIAM Journal on Applied Mathematics, 65 (2005), p. 1817.

[24] T. Chan, S. Kang, and J. Shen, *Euler's elastica and curvature-based inpainting*, SIAM Journal on Applied Mathematics, (2002), pp. 564–592.

[25] T. Chan and J. Shen, *Image Processing and Analysis: variational, PDE, wavelet, and stochastic methods*, Siam, (2005).

[26] ——, *Variational image inpainting*, Commun. Pure Appl. Math, 58 (2005), pp. 579–619.

[27] T. Chan, J. Shen, and H. Zhou, *Total variation wavelet inpainting*, Journal of Mathematical Imaging and Vision, 25 (2006), pp. 107–125.

[28] C. Chaux, P. Combettes, J. Pesquet, and V. Wajs, *A variational formulation for frame-based inverse problems*, Inverse Problems, 23 (2007), pp. 1495–1518.

[29] T. Chen and H. R. Wu, *Adaptive impulse dectection using center-weighted median filters*, IEEE Signal Processing Letters, 8 (2001), pp. 1–3.

[30] R. Coifman and D. Donoho, *Translation-invariant de-noising*, Lecture Notes in Statistics-New York-Springer Verlag, (1995), pp. 125–125.

[31] P. Combettes and V. Wajs, *Signal recovery by proximal forward-backward splitting*, Multiscale Modeling and Simulation, 4 (2006), pp. 1168–1200.

[32] I. Daubechies, *Ten lectures on wavelets*, vol. CBMS-NSF Lecture Notes, SIAM, nr. 61, Society for Industrial Mathematics, 1992.

[33] I. Daubechies, B. Han, A. Ron, and Z. Shen, *Framelets: Mra-based constructions of wavelet frames*, Applied and Computational Harmonic Analysis, 14 (2003), pp. 1–46.

[34] I. Daubechies, G. Teschke, and L. Vese, *Iteratively solving linear inverse problems under general convex constraints*, Inverse Problems and Imaging, 1 (2007), p. 29.

[35] M. Defrise and R. Clack, *A cone-beam reconstruction algorithm using shift-variant filtering and cone-beam backprojection*, IEEE Transactions on Medical Imaging, 13 (1994), pp. 186–195.

[36] B. Dong, J. Li, and Z. Shen, *X-ray ct image reconstruction via wavelet frame based regularization and radon domain inpainting*, Journal of Scientific Computing, 54(2-3) (2013), pp. 333–349.

[37] B. Dong and Z. Shen, *MRA Based Wavelet Frames and Applications*, IAS Lecture Notes Series, Summer Program on "The Mathematics of Image Processing", Park City Mathematics Institute, (2010).

[38] Y. Dong, R. F. Chan, and S. Xu, *A detection statistic for random-valued impulse noise*, IEEE Transactions on Image Processing, 16 (2007), pp. 1112–1120.

[39] D. Donoho, *De-noising by soft-thresholding*, IEEE transactions on information theory, 41 (1995), pp. 613–627.

[40] J. Eckstein and D. Bertsekas, *On the douglas-rachford splitting method and the proximal point algorithm for maximal monotone operators*, Mathematical Programming, 55 (1992), pp. 293–318.

[41] M. Elad, J. Starck, P. Querre, and D. Donoho, *Simultaneous cartoon and texture image inpainting using morphological component analysis (MCA)*, Applied and Computational Harmonic Analysis, 19 (2005), pp. 340–358.

[42] E. Esser, *Applications of Lagrangian-based alternating direction methods and connections to split Bregman*, CAM Report, 9 (2009), p. 31.

[43] M. Fadili, J. Starck, and F. Murtagh, *Inpainting and zooming using sparse representations*, The Computer Journal, 52 (2009), p. 64.

[44] L. Feldkamp, L. Davis, and J. Kress, *Practical cone-beam algorithm*, J. Opt. Soc. Am. A, 1 (1984), pp. 612–619.

[45] J. Friedman, T. Hastie, H. Höfling, and R. Tibshirani, *Pathwise coordinate optimization*, The Annals of Applied Statistics, 1 (2007), pp. 302–332.

[46] D. Gabay and B. Mercier, *A dual algorithm for the solution of nonlinear variational problems via finite element approximation*, Computers & Mathematics with Applications, 2 (1976), pp. 17–40.

[47] G. Gilboa and S. Osher, *Nonlocal operators with applications to image processing*, Multiscale Model Sim, 7 (2008), pp. 1005–1028.

[48] R. Glowinski and P. Le Tallec, *Augmented Lagrangian and operator-splitting methods in nonlinear mechanics*, Society for Industrial Mathematics, 1989.

[49] T. Goldstein, X. Bresson, and S. Osher, *Geometric applications of the split bregman method: Segmentation and surface reconstruction*, Journal of Scientific Computing, 45(1-3) (2010), pp. 272–293.

[50] T. Goldstein and S. Osher, *The split Bregman algorithm for L1 regularized problems*, SIAM Journal on Imaging Sciences, 2 (2009), pp. 323–343.

[51] R. Gordon, R. Bender, and G. Herman, *Algebraic Reconstruction Techniques (ART) for three-dimensional electron microscopy and X-ray photography* 1*, Journal of theoretical Biology, 29 (1970), pp. 471–481.

[52] G. Healey and R. Kondepudy, *Radiometric ccd camera calibration and noise estimation*, IEEE Trans. PAMI, 16 (1994), pp. 267–276.

[53] H. Hwang and R. Haddad, *Adaptive median filters: new algorithms and results*, IEEE Transactions on Image Processing, 4 (1995), pp. 499–502.

[54] H. Ji, Z. Shen, and Y. Xu, *Wavelet frame based image restoration with missing/damaged pixels*, East Asia Journal on Applied Mathematics, 1 (2011), pp. 108–131.

[55] H. Ji and K. Wang, *Robust image deconvolution with inaccurate blur kernels*, IEEE Transactions on Image Processing, 21(4) (2012), pp. 1624–1634.

[56] R.-Q. Jia, *Convergence rates of cascade algorithms*, Proceedings of American Mathematicical Society, 131 (2003), pp. 1739–1749.

[57] ——, *Approximation with scaled shift-invariant spaces by mean of quasi-projection operators*, Journal of Approximation Theory, 131 (2004), pp. 30–46.

[58] X. Jia, B. Dong, Y. Lou, and S. Jiang, *GPU-based iterative cone-beam CT reconstruction using tight frame regularization*, Physics in Medicine and Biology, 56 (2011), pp. 3787–3807.

[59] X. Jia, Y. Lou, R. Li, W. Song, and S. Jiang, *GPU-based fast cone beam CT reconstruction from undersampled and noisy projection data via total variation*, Medical physics, 37 (2010), p. 1757.

[60] L. Li, Z. Chen, Y. Xing, L. Zhang, K. Kang, and G. Wang, *A general exact method for synthesizing parallel-beam projections from cone-beam projections via filtered backprojection*, Phys Med Biol, 51 (2006), pp. 5643–5654.

[61] Z. Luo and P. Tseng, *On the convergence of the coordinate descent method for convex differentiable minimization*, Journal of Optimization Theory and Applications, 72 (1992), pp. 7–35.

[62] Y. Meyer, *Oscillating patterns in image processing and nonlinear evolution equations: the fifteenth Dean Jacqueline B. Lewis memorial lectures*, Amer Mathematical Society, 2001.

[63] M. Nikolova, *A variational approach to remove outliers and impulse noise*, Journal of Mathematical Imaging and Vision, 20 (2004), pp. 99–120.

[64] F. Noo, C. Bernard, F. Litt, and P. Marchot, *A comparison between filtered backprojection algorithm and direct algebraic method in fan beam ct*, Signal Process, 51 (1996), pp. 191–199.

[65] S. Osher and R. Fedkiw, *Level set methods and dynamic implicit surfaces*, Springer, 2003.

[66] S. K. Patch, *Computation of unmeasured third-generation vct views from measured views*, IEEE Transactions on Medical Imaging, 21-7 (2002), pp. 801–13.

[67] J. Radon, *Über die Bestimmung von Funktionen durch ihre Integralwerte längs gewisser Mannigfaltigkeiten*, Berichte Sächsische Akademie der Wissenschaften, 69 (1917), pp. 262–267.

[68] A. Ron and Z. Shen, *Affine Systems in $L_2(\mathbb{R}^d)$: The Analysis of the Analysis Operator*, Journal of Functional Analysis, 148 (1997), pp. 408–447.

[69] L. Rudin, S. Osher, and E. Fatemi, *Nonlinear total variation based noise removal algorithms*, Phys. D, 60 (1992), pp. 259–268.

[70] G. Sapiro, *Geometric partial differential equations and image analysis*, Cambridge Univ Pr, 2001.

[71] W. Segars, D. Lalush, and B. Tsui, *A realistic spline-based dynamic heart phantom*, Nuclear Science, IEEE Transactions on, 46 (1999), pp. 503–506.

[72] ——, *Modeling respiratory mechanics in the MCAT and spline-based MCAT phantoms*, Nuclear Science, IEEE Transactions on, 48 (2001), pp. 89–97.

[73] W. Segars, B. Tsui, D. Lalush, E. Frey, M. King, and D. Manocha, *Development and application of the new dynamic Nurbs-based Cardiac-Torso (NCAT) phantom.*, Biomedical 5 Engineering, (Chapel Hill, NC: University of North Carolina), (2001).

[74] I. W. Selesnick, *Smooth wavelet tight frames with zero moments*, Applied and Computational Harmonic Analysis, 10 (2001), pp. 163–181.

[75] S. Setzer, *Split Bregman algorithm, Douglas-Rachford splitting and frame shrinkage*, Scale Space and Variational Methods in Computer Vision, (2009), pp. 464–476.

[76] Z. Shen, *Wavelet frames and image restorations*, Proceedings of the International Congress of Mathematicians, Hyderabad, India, (2010).

[77] Z. Shen and Z. Xu, *On b-spline framelets derived from the unitary extension principle*, SIAM Journal on Mathematical Analysis, 45(11) (2013), pp. 127–151.

[78] R. L. Siddon, *Fast calculation of the exact radiological path for a 3-dimensional ct array*, Medical Physics, 12 (1985), pp. 252–5.

[79] E. Sidky, C. Kao, and X. Pan, *Accurate image reconstruction from few-views and limited-angle data in divergent-beam CT*, Journal of X-Ray Science and Technology, 14 (2006), pp. 119–139.

[80] E. Sidky and X. Pan, *Image reconstruction in circular cone-beam computed tomography by constrained, total-variation minimization*, Physics in medicine and biology, 53 (2008), p. 4777.

[81] J. Starck, M. Elad, and D. Donoho, *Image decomposition via the combination of sparse representations and a variational approach*, IEEE transactions on image processing, 14 (2005), pp. 1570–1582.

[82] X. Tai and C. Wu, *Augmented Lagrangian method, dual methods and split Bregman iteration for ROF model*, Scale Space and Variational Methods in Computer Vision, (2009), pp. 502–513.

[83] P. Tseng, *Convergence of a block coordinate descent method for nondifferentiable minimization*, Journal of optimization theory and applications, 109 (2001), pp. 475–494.

[84] P. Tseng and S. Yun, *A coordinate gradient descent method for nonsmooth separable minimization*, Mathematical Programming, 117 (2009), pp. 387–423.

[85] Y. Ye, H. Yu, Y. Wei, and G. Wang, *A general local reconstruction approach based on a truncated hilbert transform*, International Journal of Biomedical Imaging, (Article ID: 63634, 8 pages, 2007).

[86] H. Yu and G. Wang, *Compressed sensing based interior tomography*, Physics in Medicine and Biology, 54(9) (2009), pp. 2791–2805.

[87] H. Yu, Y. Wei, J. Hsieh, and G. Wang, *Data consistency based translational motion artifact reduction in fan-beam CT*, Medical Imaging, IEEE Transactions on, 25 (2006), pp. 792–803.

[88] H. Yu, Y. Ye, S. Zhao, and G. Wang, *Local roi reconstruction via generalized fbp and bpf algorithms along more flexible curves*, International Journal of Biomedical Imaging, (2006), pp. 1–7.

[89] H. Yu, S. Zhao, A.Hoffman, and G. Wang, *Ultra-low dose lung ct perfusion regularized by a previous scan*, Academic Radiology, 16(3) (2009), pp. 363–373.

[90] H. R. S. Z. Wang, A. C. Bovik and E. P. Simoncelli, *Image quality assessment: From error visibility to structural similarity*, IEEE Transactions on Image Processing, 13(4) (2004), pp. 600–612.

[91] X. Zhang, M. Burger, X. Bresson, and S. Osher, *Bregmanized nonlocal regularization for deconvolution and sparse reconstruction*, SIAM Journal on Imaging Sciences, 3 (2010), pp. 253–276.

WAVELET APPROXIMATION AND IMAGE RESTORATION

LI JIA

NATIONAL UNIVERSITY OF SINGAPORE

2013